CB-NOTE 303 15.5.1997

Analysis of the channel $\bar{\mathrm{p}}\mathrm{p} \to \mathrm{K}^{\pm}\pi^{\mp}\mathrm{K}_L$ in $\bar{\mathrm{p}}$ annihilation at rest

Technical report

Matthias Heinzelmann
Stefan Spanier

University of Zürich

Abstract

This note describes the preparation of the Dalitz plot for the reaction $\bar{\mathrm{p}}\mathrm{p} \to \mathrm{K}^{\pm}\pi^{\mp}\mathrm{K}_L$ at rest from 2-prong triggered data. Minimum bias data were used for an estimate of the branching ratio. Major part of the work is the diploma thesis of Matthias.

Contents

1 Introduction **4**

2 Trigger **4**

3 Software **5**

4 Selection **5**
- 4.1 JDC . . . 5
- 4.2 Barrel . . . 6
- 4.3 K_L missing mass window . . . 9
- 4.4 Total energy cut . . . 10
- 4.5 Anti-K_SK_L cut . . . 11
- 4.6 Separation of the hypothesis by $\boldsymbol{dE/dx}$ . . . 11
  - 4.6.1 Calibration . . . 12
  - 4.6.2 Selection . . . 14
- 4.7 Kinematic fit . . . 15
- 4.8 Summary of the selection . . . 17

5 Monte Carlo **19**
- 5.1 Selection . . . 19
- 5.2 Acceptance . . . 20
- 5.3 Acceptance correction for $\boldsymbol{K_L}$ interacting . . . 22
  - 5.3.1 Selection of $\boldsymbol{K_L K_S \pi^0}$ . . . 23
  - 5.3.2 Topology of the K_L PEDs . . . 25
  - 5.3.3 K_L(interacting) in the Monte Carlo . . . 27
  - 5.3.4 Acceptance correction . . . 29
- 5.4 Branching ratio . . . 30
- 5.5 Background . . . 31
  - 5.5.1 $\bar{p}p \to K^{\pm}\boldsymbol{\pi^{\mp}}K_{\boldsymbol{L}}$, $K^{\pm} \to \boldsymbol{\mu^{\pm}\nu}$ . . . 32
  - 5.5.2 $\bar{p}p \to \boldsymbol{\pi^+\pi^-\pi^0}$ . . . 32
  - 5.5.3 $\bar{p}p \to \boldsymbol{\pi^+\pi^-\eta}$ . . . 32
  - 5.5.4 $\bar{p}p \to K^+K^-$ . . . 33
  - 5.5.5 $\bar{p}p \to K_SK_L$, $K_S \to \boldsymbol{\pi^+\pi^-}$ . . . 33
  - 5.5.6 $\bar{p}p \to K^+K^-\boldsymbol{\pi^0}$ . . . 34
  - 5.5.7 $\bar{p}p \to \boldsymbol{\pi^+\pi^-\omega}$ . . . 34
  - 5.5.8 $\bar{p}p \to K^{\pm}\boldsymbol{\pi^{\mp}}K_{\boldsymbol{L}}\boldsymbol{\pi^0}$ . . . 34
  - 5.5.9 Background summary . . . 37

6 The Dalitz plot **37**

7 Partial wave analysis **41**
7.1 Transition amplitude 41
7.1.1 Spin-parity function 42
7.1.2 Dynamical function 43
7.1.3 Centrifugal barrier 43
7.1.4 Isospin decomposition 43
7.2 Fit - Procedure 46
7.3 Partial waves 48

8 PWA fits **55**

9 Discussion **58**

1 Introduction

The spectroscopy of scalar and tensor mesons is one major investigation of the Crystal Barrel experiment. We already have published the observation of the I=1 resonance $a_0(1450)$ [1] which is expected to decay to $K^0K^\pm$, $K^0\bar{K}^0$ and K^+K^-. The extraction of the I=1 scalar and tensor partial waves in the present annihilation channel is an essential input to arrive at conclusive information about $\bar{\text{K}}$K couplings for both, I=0 ($\pi\pi$ S-wave; $f_0(1500)$) and I=1 scalar resonances.

The work is devided into two main parts:

1. Data preparation
2. Partial Wave Analysis

The data selection concentrates on the pattern due to a missing K_L and two oppositely charged particles. They are characterized by two tracks starting in the liquid hydrogen targed and showing up in the PWC (SVTX) and the JDC. The channel with K_L interacting (with $\approx 50\%$ probability) has a third PED [1] but contains background from channels 2prong plus $\gamma\gamma$ with one γ from the π^0, η or η' decay not detected.

The data reconstruction started with two prong long track triggered data taken in June 1994 (about $7.8 \cdot 10^6$) which yielded about 12,000 events in the Dalitz plot. To ensure a consistent treatment not all of the 13 Mio June'94 2 prong data were used in this first step (2 different trigger setups were applied). Minimum bias data from June 1994 were analysed.

The data selection proceeds the following:

1. cuts due to topology
2. kinematic cuts
3. separation of charged π and K

2 Trigger

For the run periode 1994 the following 2 prong trigger setup was used:

```
Trigger conditions as read from DAMO bank :
PWC_1 lower,upper bound     :      2     2
PWC_2 lower,upper bound     :      2     2
JDC   lower,upper bound     :      0    15
FACE  lower,upper bound     :      0    15
```

[1] particle energy deposit

```
Name of trigger preset file   : 2-Pr;default
Name of hardware trigger      : /cb1/pro/TRIGGER/bsvp1j1.sts
Name of JDC multiplicity file : /cb1/pro/TRIGGER/j4mxx22.par
```

3 Software

For MC studies and the reconstruction the standard CBOFF code was used :

- CBOFF version 1.30/00
- LOCATER 2.01/00
- BCTRAK 2.04/00
- GTRACK 1.36/00
- CBKFIT 3.09/00
- CBGEANT 5.05/00
- GEANT 3.2130

4 Selection

The signature of the channel $K^{\pm}\pi^{\mp}K_L$ with the K_L missing: two tracks in the JDC of opposite charge sign which should show up in the barrel, too. Due to the missing K_L no additional entries in the crystals e.g. belonging to photons are expected. After matching the hit crystals to the tracks no further PEDs should remain. The charged pion and kaon can be distinguished by their differential energy loss in the JDC.

4.1 JDC

The following criteria for selecting two long tracks are applied :

1. 2 tracks in TTKS bank
2. charge sum zero
3. at least 1 hit/track above layer 20
4. at least 1 hit/track below layer 4
5. more than 9 hits/track
6. χ^2 per d.o.f. of a track lower than 1.2 (good track)

So we arrive at a data sample of good two prong long track events of 5,598,275 events.

cut no.		remaining events
	events on tape	7,720,872
1.	2 tracks in TTKS	6,837,591
2.	charge sum zero	6,599,505
3.	1 hit above layer 20	6,151,781
4.	1 hit below layer 4	5,814,748
5.	more than 9 hits	5,808,287
6.	$\chi^2 < 1.2$	5,598,275

Table 1: Selection based on JDC information.

4.2 Barrel

The pre-settings for the reconstruction were the following :

minimum energy for xtal in 'TBEN'	EMINBC	0.8 MeV
minimum energy of cluster	ECLUBC	4.0 MeV
minimum energy for xtal in 'TBCL'	EXTLBC	1.0 MeV
minimum energy of PED	EPEDBC	10.0 MeV
minimum energy to start a cluster	ECLSBC	4.0 MeV
subtract pedestals	QSUBBC	.true.

In addition to this standard definition of a PED in the Crystal Barrel offline software the following criteria have to be fulfilled: The energy of the central crystal (E_1) of a PED has to be greater than 13 MeV. The ratio of this energy to the sum of the energy in the next eight neighbours including the central one (E_9) has to be $\frac{E_1}{E_9} < 0.96$. Split-off PEDs were identified by DOLBY-C [2].
Now one has to find the PEDs which belong to the two charged particles as they deposit energy in the crystals. A PED is considered matched to a track if the angle θ between the shower direction of this PED and track extrapolated to the barrel entry fulfils the condition : $\cos(\theta) > 0.98$. This method finds to 99.4 % of all tracks a corresponding PED. Additional PEDs in the same cluster are considered as matched, too (cluster matching). Information about matched tracks is provided by the offline code.
PEDs which belong to a track can be found using the TAXI algorithm [3]. In our case the use of the TAXI algorithm recovers 11 % of events with no un-

matched PED compared to the cluster matching. The distribution of the number of unmatched PEDs after applying the matching criteria is shown in fig. 1.

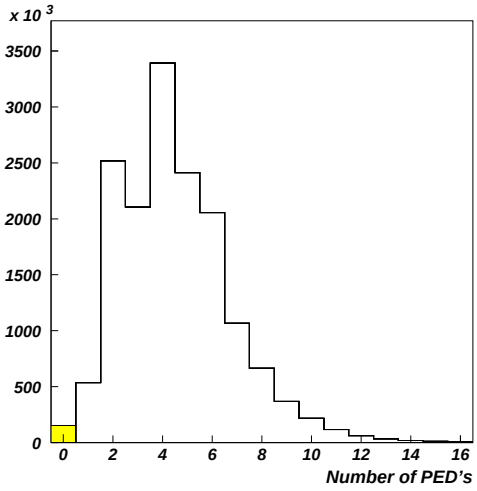

Figure 1:
Number of PEDs after matching.

Of course, too many PEDs are rejected by the matching procedures. There are 'cluster matched' PEDs which can be combined to a π^0 or η, and most probably belong to background channels ($\pi^+\pi^-\pi^0$, $\pi^+\pi^-\eta$ and $\mathrm{K}^+\mathrm{K}^-\pi^0$; see section background 5.5). The $\gamma\gamma$ invariant mass of all PEDs not explicitely connected to the tracks by the $\cos(\theta)$ criterium is shown in figure 2. Clearly visible is a π^0 peak. The η peak is dominated by a large combinatorial background. An event is rejected whenever one or more combinations of the $\gamma\gamma$ invariant mass mm fall into a mass window $mm \in [105, 165]$ MeV/c^2 for π^0, and $mm \in [500, 600]$ MeV/c^2 for the η . The missing mass spectrum of the rejected events is displayed in figure. 3. The majority of events rejected does not come from the one missing K_L region.

cut no.		remaining events
	2 long tracks	5,598,275
1.	0 unmatched PEDs	156,229
2.	no π^0 or η combination	132,846

Table 2: Selection based on information from the crystals.

We end up with 132,846 events. The missing mass spectrum of all accepted 0 PED events is shown in figure 4. Both charged particles are treated as pions. Therefore one expects the peak of the signal channel (hatched region) to be

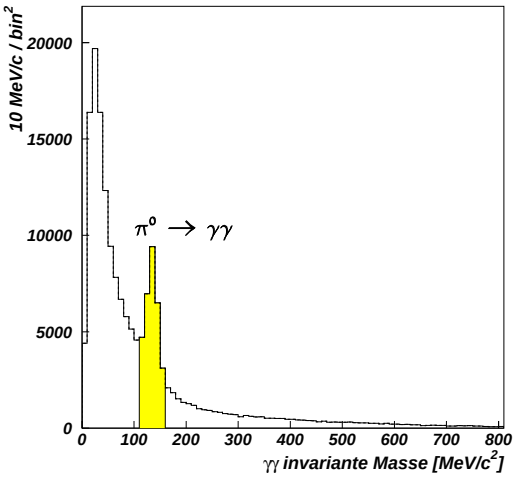

Figure 2:
The $\gamma\gamma$ invariant mass of all PEDs not explititely connected to the tracks. A π^0 signal mismatched to a track can be seen.

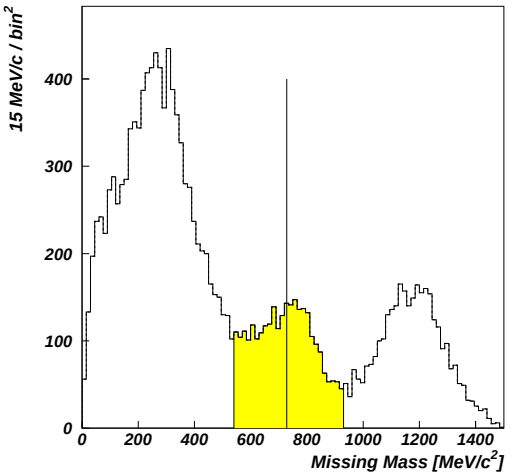

Figure 3:
The $\pi^+\pi^-$ missing mass for the rejected events due to the π^0 / η cut. To identify the structures see fig. 4.

centered at 728 MeV. In addition one observes the collinear events $\pi^+\pi^-$, K^+K^- and the $\pi^+\pi^- K_L K_L$ events with two K_L not detected. The fit of a gaussian plus a polynom of first degree to the K_L signal yields about 12,000±600 $K^{\pm}\pi^{\mp}K_L$ events.

In fig. 5 the total momentum of the remaining events is plotted against the total energy (all charged particles are treated as pions). The marked areas are populated dominantely the following:

A : completely reconstructed events
$\pi^+\pi^-$ (E_{tot} = 1877 MeV; p_{tot} = 0 MeV/c) and
K^+K^- (E_{tot} = 1620 MeV; p_{tot} = 0 MeV/c)

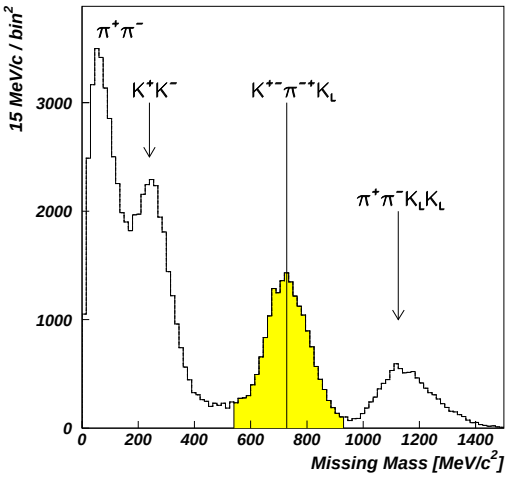

Figure 4:
The $\pi^+\pi^-$ missing mass after the preselection : two long tracks and no additional PEDs in the barrel.

B : $K^{\pm}\pi^{\mp}K_L$ with one K_L missing
The events are seen as a characteristic band which spans the allowed momentum range from 0 to 747 MeV/c of the K_L. The enhancement at a K_L momentum of 615 MeV/c is due to events from the reaction $\bar{p}p \to K^*K_L$; $K^* \to K^{\pm}\pi^{\mp}$.

C : K_SK_L with K_L missing
The K_S decays into $\pi^+\pi^-$ resulting in a 2prong event, if the K_L is missing ($E_{tot} = 938$ MeV; $P_{tot} = 798$ MeV/c).

D : two K_L missing
Well separated from the $K^{\pm}\pi^{\mp}K_L$ events one sees the $\pi^+\pi^-K_LK_L$ events. Both K_L do not interact with the crystals. The border line of region D corresponds to a missing mass of two K_L exactly.

E : missing π^0
$\pi^+\pi^-\pi^0$ events with 2γ missing which belong to a π^0 are found here. The dashed line in region E marks the position of events with a π^0 missing.

The final states $\pi^+\pi^-\pi^0$ K_SK_L and K^+K^- appear in the kinematic neighbourhood of the signal and therefore are potential background channels.

4.3 K_L missing mass window

Since we are looking for $K^{\pm}\pi^{\mp}K_L$ events with the K_L missing the missing $K^+\pi^-$ or $K^-\pi^+$ mass has to be at about M(K_L). As we don't yet know which combination is correct we try both hypotheses. An event is accepted if it has at least one entry in the mass window:

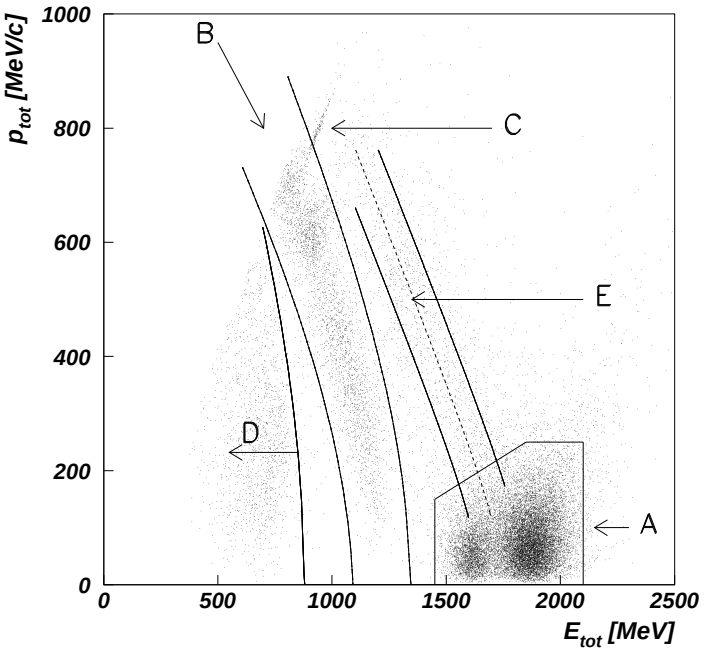

Figure 5: Total energy and total momentum. For the calculation of the energy all charged particles were assumed to be pions. For explanation of the regions see the text. Region B corresponds to the $\mathrm{K}^{\pm}\pi^{\mp}\mathrm{K}_L$ events.

$$350\,\mathrm{MeV}/c^2 \leq \left\{ \begin{array}{c} \text{Missing Mass } K^+\pi^- \\ or \\ \text{Missing Mass } K^-\pi^+ \end{array} \right\} \leq 650\,\mathrm{MeV}/c^2. \qquad (1)$$

In fig. 6 the missing mass of all accepted events is shown (17,524 events; 5,526 events have one, 11,998 events have two entries in the mass window.). The asymmetry in the K_L peak is due to the combinatorial background: high momentum particles have an enhanced probability for two entries in the window.

4.4 Total energy cut

To reduce background mainly caused by badly reconstructed $\mathrm{K}^+\mathrm{K}^-$ events a cut is applied to the total energy. Events were accepted if the total energy was lower

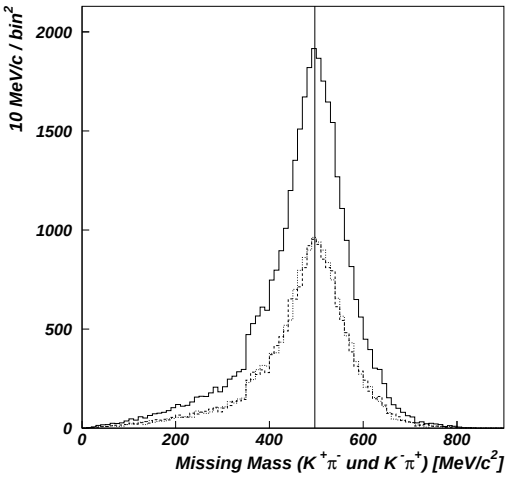

Figure 6:
The $K^{\pm}\pi^{\mp}$ missing mass distribution after the cut for one missing K_L. The line marks the nominal mass of K_L. The lower distributions are $K^+\pi^-K_L$ (dashed) and $K^-\pi^+K_L$ (dotted).

than 1400 MeV (corresponds to about $2 * m_p - m_{K_L}$). An amount of 17,265 events remained.

4.5 Anti-K_SK_L cut

As one recognizes in figure 5, K_SK_L events with the K_S decaying into $\pi^+\pi^-$ are kinematically close to the $K^{\pm}\pi^{\mp}K_L$ events. The cosinus of the opening angle between the two decay pions of the K_S is expected to lie between 0.3 and 0.6. The average decay length of the K_S is 4.3 cm leading to a secondary vertex. To reduce feedthrough from K_SK_L events a cut against the opening angle of the tracks and the distance of the secondary vertex from the center was applied :

$$\begin{gathered} 0.1 < \cos(\theta) < 0.7 \\ \text{and} \\ \text{radius of intersection point of the two tracks in the xy-plane} \\ \text{outside the target} : r_{xy} > 1.2\ cm. \end{gathered} \tag{2}$$

The cut was optimized using Monte Carlo events. 17,208 events remain.

4.6 Separation of the hypothesis by dE/dx

Kinematic cuts already well define the final state. The next step is to separate $K^+\pi^-K_L$ from $K^-\pi^+K_L$ and both from remaining K^+K^-X or $\pi^+\pi^-X$ events. To distinguish the different possibilities the information from dE/dx is used. Figure 7 shows momentum versus dE/dx for the 17,208 events accepted. The two bands of the pions and the kaons are clearly visible and a third band which appears for positive particles only and is due to protons. For momenta lower than about 450

MeV/c a destinction of kaons and pions with a probability greater than 97% is possible using the χ^2-method. In this lower momentum region we find 76% of all events. For momenta above 450 MeV/c it is possible to confound $K_L K^+ \pi^-$ with $K_L K^- \pi^+$. According to the Monte Carlo simulation less than (0.75± 0.05%) of the events are assigned to the wrong hypothesis. For the dE/dx calibration an identical procedure is applied for data and Monte Carlo. It is described in the next section.

4.6.1 Calibration

Figure 8 shows the dE/dx distribution for momenta between 440 and 460 MeV/c. One would expect a sum of two Landau distributions. However, due to the applied truncated mean method [4] and the limited amplitude (dE/dx) and momentum resolution they can be approximated with two gaussians. The separation can be made up to 1.5 σ of the two gaussians.

The maximum momentum of charged particles in the channel under consideration is 750 MeV/c. Therefore a simplified Bethe-Bloch formula is used:

$$-\left(\frac{dE}{dx}\right)_{(theo)} = \frac{M}{\beta^2}\left[\ln\frac{N\cdot\beta^2}{1-\beta^2} - \beta^2\right]. \tag{3}$$

This function was fitted to $\pi^+\pi^-\pi^0$ and $K^+K^-\pi^0$ data (and separatly to the corresponding Monte Carlo data) for either pions and kaons. Coefficients for the protons were calculated since the statistics for the protons was too low to be fit. The calibration of the June'94 data revealed:

$$\begin{array}{llll} M_\pi = (1.747 \pm 0.001)\times 10^{-4} & N_\pi = (2.16 \pm 0.19)\times 10^{8} & \text{for pions.} \\ M_K = (3.424 \pm 0.005)\times 10^{-4} & N_K = (7.44 \pm 1.00)\times 10^{3} & \text{for kaons.} \end{array}$$

These dE/dx functions (shown as lines in fig. 7) are used to calculate a χ^2 for the particle hypothesis π ,K or p:

$$\begin{aligned} \chi^2_{\pi^\pm} &= \left(\frac{dE/dx_{(theo,\pi)} - dE/dx_{(measured)}}{\sigma_{dE/dx}}\right)^2 \\ \chi^2_{K^\pm} &= \left(\frac{dE/dx_{(theo,K)} - dE/dx_{(measured)}}{\sigma_{dE/dx}}\right)^2 . \end{aligned} \tag{4}$$

From the fit of Gaussians to the dE/dx distributions in different β intervals we derived a $\sigma_{\mathrm{dE/dx}} = \mathrm{dE/dx}_{theo} \times 0.142$.

The Monte Carlo data were calibrated with the same method. There was a momentum dependent discrepancy observed compared to data, different for pions and kaons (see fig.9). The deviations were corrected relatively to the June'94 data.

This allowed the application of the same theoretical dE/dx functions eqn. 3. Also the dE/dx resolution was adjusted to the June'94 data.

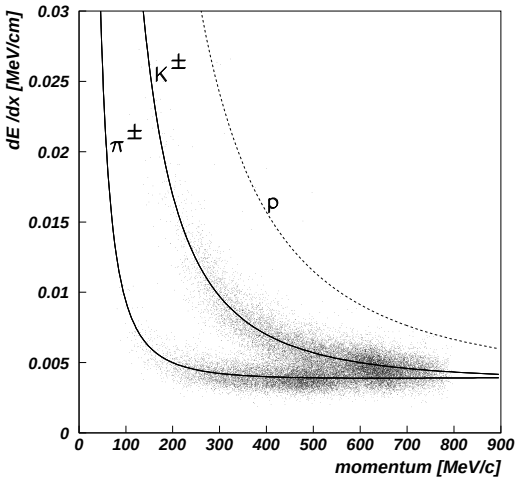

Figure 7:
The dE/dx for all 17,208 events with at least one entry in the missing mass window.

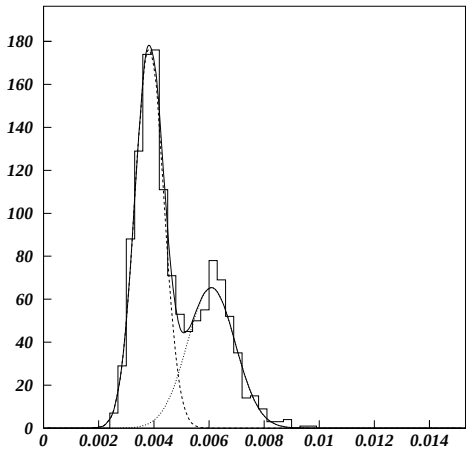

Figure 8:
The dE/dx distribution for the events with a momentum between 440 MeV/c and 460 MeV/c.

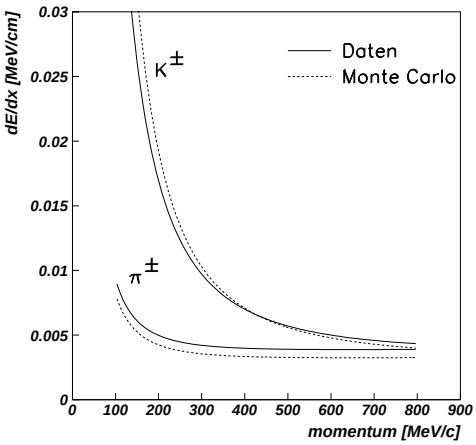

Figure 9: Fitted Bethe-Bloch-functions for Juni'94 data (solid line) and Monte Carlo data (dashed line).

4.6.2 Selection

All events containing a proton according to the dE/dx - χ^2 are rejected. In the next step, for each event the χ^2 are combined the following:

$$\begin{aligned} \chi^2_{\pi^+\pi^-} &= \chi^2_{\pi^+} + \chi^2_{\pi^-} \\ \chi^2_{\pi^+\mathrm{K}^-} &= \chi^2_{\pi^+} + \chi^2_{\mathrm{K}^-} \\ \chi^2_{\mathrm{K}^+\pi^-} &= \chi^2_{\mathrm{K}^+} + \chi^2_{\pi^-} \\ \chi^2_{\mathrm{K}^+\mathrm{K}^-} &= \chi^2_{\mathrm{K}^+} + \chi^2_{\mathrm{K}^-} \ . \end{aligned} \tag{5}$$

Hence, the signal events are defined the following:

$$\begin{aligned} \mathrm{K}^-\pi^+\mathrm{K}_L \ : \quad \chi^2_{\mathrm{K}^+\pi^-} &< \chi^2_{\pi^+\mathrm{K}^-} \ and \ \chi^2_{\pi^+\pi^-} \ and \ \chi^2_{\mathrm{K}^+\mathrm{K}^-} \ , \\ \mathrm{K}^+\pi^-\mathrm{K}_L \ : \quad \chi^2_{\pi^+\mathrm{K}^-} &< \chi^2_{\mathrm{K}^+\pi^-} \ and \ \chi^2_{\pi^+\pi^-} \ and \ \chi^2_{\mathrm{K}^+\mathrm{K}^-} \ . \end{aligned} \tag{6}$$

In table 3 the classification due to the dE/dx is summarized. 12,670 events were selected as $\mathrm{K}^\pm\pi^\mp\mathrm{K}_L$; 256 events contradict the classification of the missing mass cut.

	$\mathrm{K}^+\pi^-\mathrm{K}_L$	$\pi^+\mathrm{K}^-\mathrm{K}_L$	$\pi^+\pi^-X$	$\mathrm{K}^+\mathrm{K}^-X$
events	6430	6240	3280	1002

Table 3: Classification using dE/dx.

4.7 Kinematic fit

After the separation of the hypothesis into $K^+\pi^-K_L$ and $K^-\pi^+K_L$ based on the dE/dx a kinematic fit CBKFIT [5] was applied.
In the June 1994 run all transversal momenta (p_{xy}) of charged particles are measured 0.5% too low. Therefore, before fitting we scale the momenta the following: $p'_{xy} = 1.005 * p_{xy}$

Also the errors of the three charged particle track parameters have to be corrected:

- Ψ : track direction at the origin,
- α : track curvature ($= \frac{1}{p_{xy}}$),
- $\tan\lambda$: slope of the track helix with respect to the detector z-axis.

All three σ are scaled by a factor 1.3. This is established with the $\pi^+\pi^-\pi^0$ and $K^+K^-\pi^0$ data samples of the considered run-period. For the $K^\pm\pi^\mp K_L$ data the pulls the confidence level distributions are shown in figure 10. Events with a confidence level greater 10%, either being $K^-\pi^+K_L$ or $K^+\pi^-K_L$, were accepted. After the cut on dE/dx and the kinematic fit an amount of 11,373 events remained.

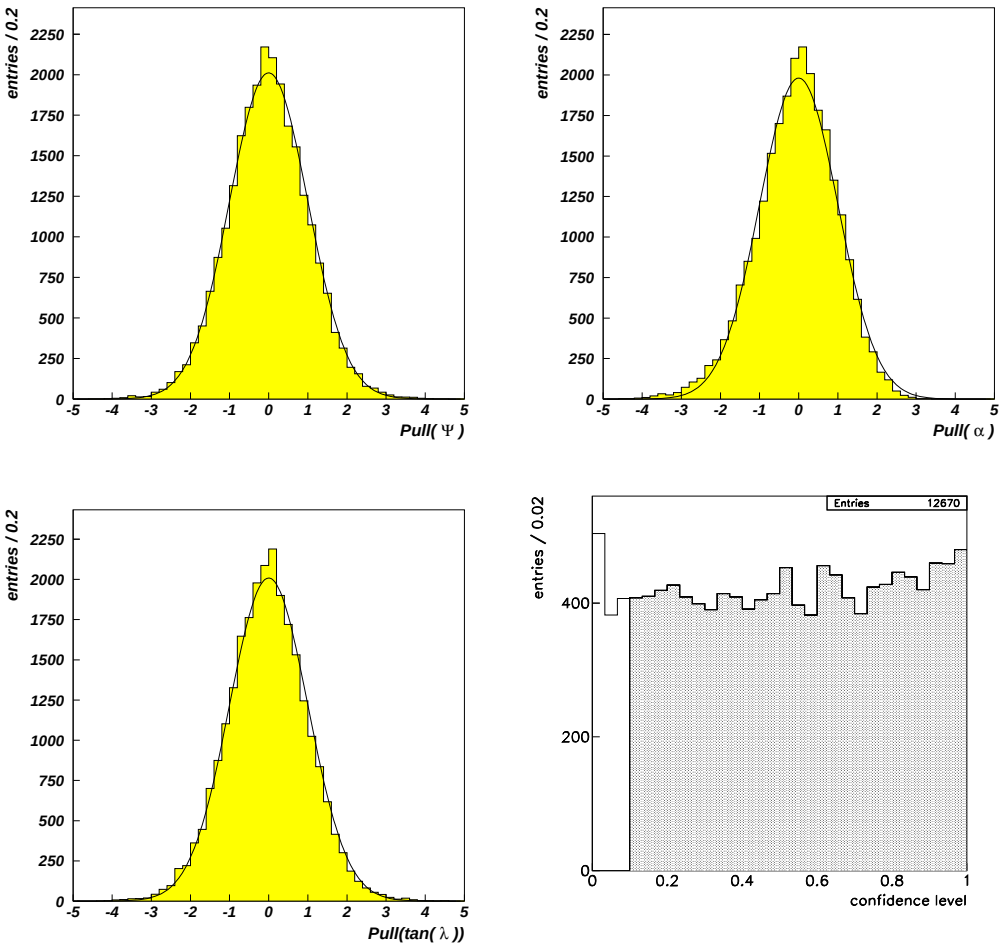

Figure 10: Distribution of the pulls and the confidence level for the June'94 data (both hypotheses added together). Both hypotheses are added together. The solid line is the expected Gaussian with $\sigma = 1$ and mean at 0.

4.8 Summary of the selection

Cut				remaining events
	events on tape			7'720'872
(6)	2 long tracks			5'598'275
(8)	0 PED's			132'846
(9)	350 MeV/$c^2 \leq$ missing mass $\leq$ 650 MeV/c^2			17'524
(10)	$E_{tot}(K^{\pm}\pi^{\mp}) \leq 1400$ MeV, K_S Cut			17'208
		$K^-\pi^+K_L$	$K^+\pi^-K_L$	
(11)	$\chi^2_{dE/dx}(K^{\pm}\pi^{\mp})$ beste Hypothese	6'430	6'240	12'670
(12)	cl($K^{\pm}\pi^{\mp}K_L$) $\geq$ 10 %	5'774	5'599	11'373

Table 4: Selection of the $K^{\pm}\pi^{\mp}K_L$ final state.

There is a small difference between the number of $K_LK^+\pi^-$ (5774) and $K_LK^-\pi^+$ (5599) events. The origin of the asymmetry is established in CB-Note 310 : the different cross sections of K^+ and K^- for reactions with protons in the hydrogen target and with the nuclei in the CsI(Tl)-crystal are responsible for the slight difference. Important to note, that the difference is momentum dependent only below 250 MeV/c kaon-momentum, as will be demonstrated below.

The asymmetry in each Dalitz plot cell $i = (m^2_{12}, m^2_{13})$ considering the statistics is given in terms of a χ^2_i. With $N^{\pm}_i$ the number of events $n^{\pm}_i$ per cell normalized to all events in the Dalitz plot:

$$\chi^2_i = \frac{(N^-_i - N^+_i)^2}{\sigma^2_{N^-_i} + \sigma^2_{N^+_i}} \cdot s \tag{7}$$

$$s = \frac{N^-_i - N^+_i}{\mid N^-_i - N^+_i \mid} \tag{8}$$

The following table shows the determination of the χ^2 for different binnings of the Dalitz plot:

binning	χ^2	N_{cells}	χ^2/N_{cells}
20x20	256.7	235	1.09
25x25	426.2	397	1.07
30x30	564.0	563	1.00
40x40	931.4	868	1.07

The signed chisquare for a 25x25 binned Dalitz plot is shown in fig. 11: The K^- excess (left) and K^+ excess (right).

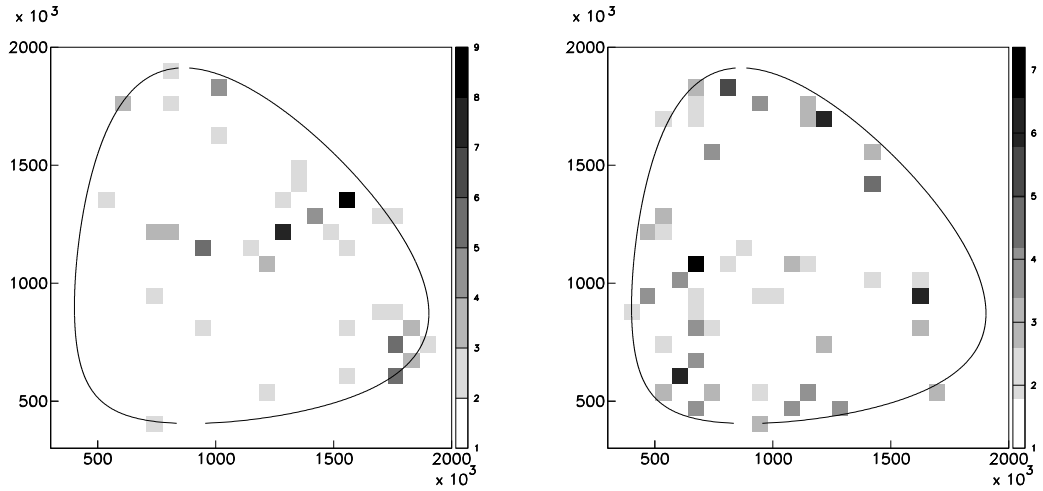

Figure 11: The chisquare comparison between the two data samples with differently charged kaons. The left plot shows the Dalitz plot cells with an excess of $K^-K_L\pi^+$, the right plot the Dalitz plot cells with an excess of $K^+K_L\pi^-$ events.

There is no closed region of significant deviations. In the K^- channel one observes a clustering for low K^- momenta. More events belonging to the $K^+K_L\pi^-$ channel in comparison to $K^-K_L\pi^+$ are found at high K^+ momentum. In fig. 12 the number of $K^-K_L\pi^+$ events is divided by the number of $K^+K_L\pi^-$ for different K-momentum regions:

$$\epsilon_\pm = \frac{N(K^-K_L\pi^+)}{N(K^+K_L\pi^-)}(p(K)) \tag{9}$$

A constant fitted to the momentum-ratio spectrum fig. 12 for momenta above 250 MeV/c gives $\epsilon_\pm = 0.94 \pm 0.02$ with a $\chi^2 = 1.16$.

According to fig. 12 (left) the small difference between $K_L K^-\pi^+$ and $K_L K^+\pi^-$ varies slowly with the charged kaon momentum: there is a small slope in the ratio $p(K^-)/p(K^+)$ which is also seen in the Monte Carlo (see there). The excess of K^- versus K^+ at low momenta ($p < 250$ MeV/c) can be explained by their different behaviour in the crystals: a K^- excites more crystals than a K^+. Because of the enlarged cluster of hit crystals the matching probability of K^- is increased against the K^+ at low momenta (see CB-Note 310). The region below 250 MeV/c kaon momentum is sparsely populated in both channels. Therefore, no further effort was put into the understanding of this phase space region. Effects concerning the charged tracking are corrected by the Monte Carlo, which will be shown in the next section.

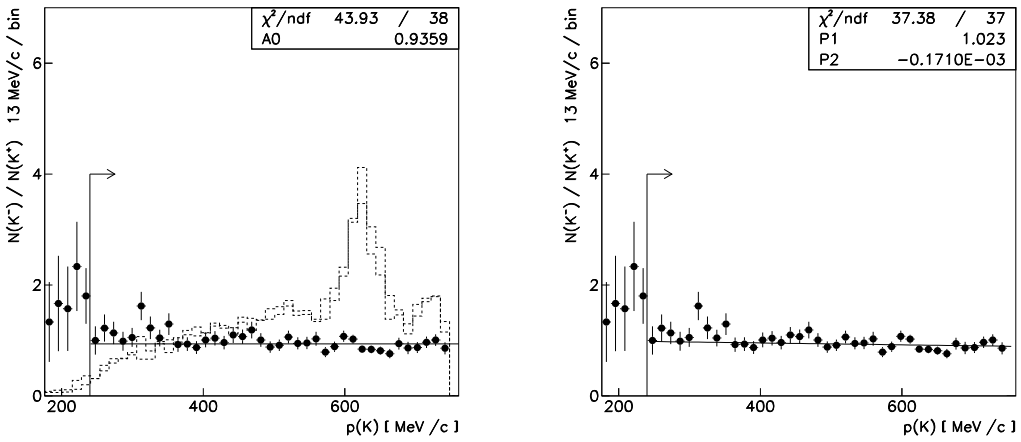

Figure 12: The ratio of K^- channel events and K^+ channel events versus momentum. The original momentum spectra are superimposed. A constant (left) and a straight line (right) were fit.

5 Monte Carlo

For the determination of the reconstruction efficiency, the acceptance and the contribution of possible background channels the CBGEANT [6] program is used.

5.1 Selection

The K_L was generated as non-interacting particle (geantino). Corrections concerning the interaction probability of the K_L in the crystals were taken from the investigations in the channel $K_L K_L \pi^0$[7]. In total 600,000 $K^\pm\pi^\mp K_L$ events were generated. The events went through the same selection chain as the data. Table 5 summarizes the selection.

The reconstruction efficiency for the channel $\bar{p}p \to K^\pm\pi^\mp K_L$ with a non-interacting K_L arrives at:

$$\epsilon_{K^\pm\pi^\mp K_L} = (14.3 \pm 0.1)\ \%. \tag{10}$$

To this reconstruction efficiency corrections for interacting K_L, which are hidden under the charged tracks, have to be applied (see section 5.3).

The asymmetry in dependence on the momentum is shown in fig. 13. The average for $p(K^-)/p(K^+) = 0.94 \pm 0.01$ compares well to the data, where we found a ratio of 0.94 ± 0.02. Also the parameters of the fitted slope correspond to the values in the data considering only momenta above 250 MeV/c and giving an average ratio of 1.

Cut		remaining events
	generated events	600'000
(6)	2 long tracks	213'718
(8)	0 PED's	146'717
(9)	350 MeV/c^2 $\leq$ missing mass $\leq$ 650 MeV/c^2	130'610
(10)	$E_{tot}(K^{\pm}\pi^{\mp}) \leq 1400$ MeV, K_S Cut	128'580
(11)	$\chi^2_{dE/dx}(K^{\pm}\pi^{\mp})$ best hypothesis	95'324
(12)	cl($K^{\pm}\pi^{\mp}K_L$) $\geq$ 10 %	85'679

Table 5: Selection of the $K^{\pm}\pi^{\mp}K_L$ Monte Carlo events.

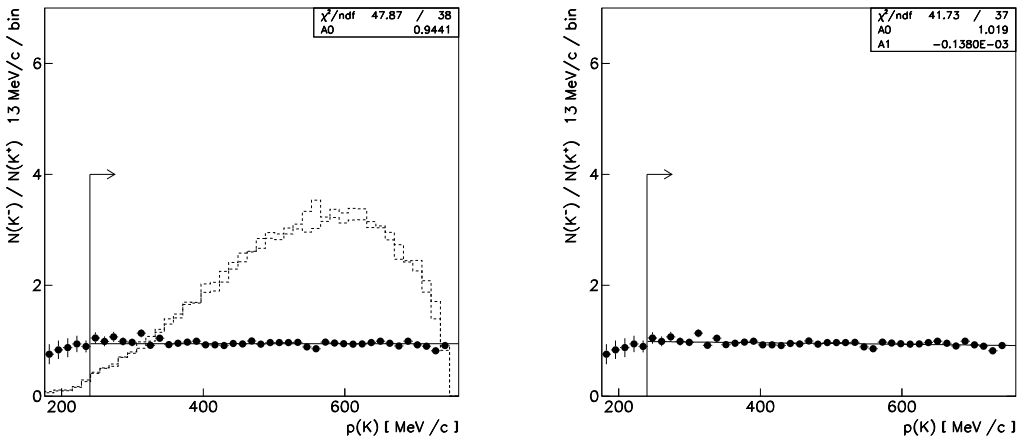

Figure 13: The ratio of K^- channel events and K^+ channel events versus momentum. The selected Monte Carlo spectra are superimposed. A constant (left) and a straight line (right) were fit.

5.2 Acceptance

The interaction probability as a function of the K_L-momentum is parametrized the following [7]:

$$P^{int} = A + (1 - A)e^{-p(K_L)/B} \tag{11}$$

with $A = 0.50 \pm 0.01$ and $B = (145 \pm 28)\,\mathrm{MeV}/c$. The function leads to the interaction probability of (54 ± 4) % averaged over the whole phase space.

The survival probability for the K_L is given as:

$$P^{surv} = e^{-r_0/c\gamma\beta\tau} \ , \tag{12}$$

with $r_0 = 0.4$ m the mean distance between target and crystals, β the velocity and $\tau = 5.1 \times 10^{-8} s$ the lifetime of the K_L.

The $K^{\pm}\pi^{\mp}$ identification probability $P^{K^{\pm}\pi^{\mp}}$ ($\epsilon_{K^{\pm}\pi^{\mp}K_L}$) results from section 5.1. The acceptance for each Dalitz plot cell is calculated the following:

$$P^{acc} = P^{K^{\pm}\pi^{\mp}} \times (1 - P^{int}) \times P^{surv} \ . \tag{13}$$

The combined acceptance P^{acc} for the channel $\bar{p}p \to K^{\pm}\pi^{\mp}K_L$ is displayed in fig. 14.

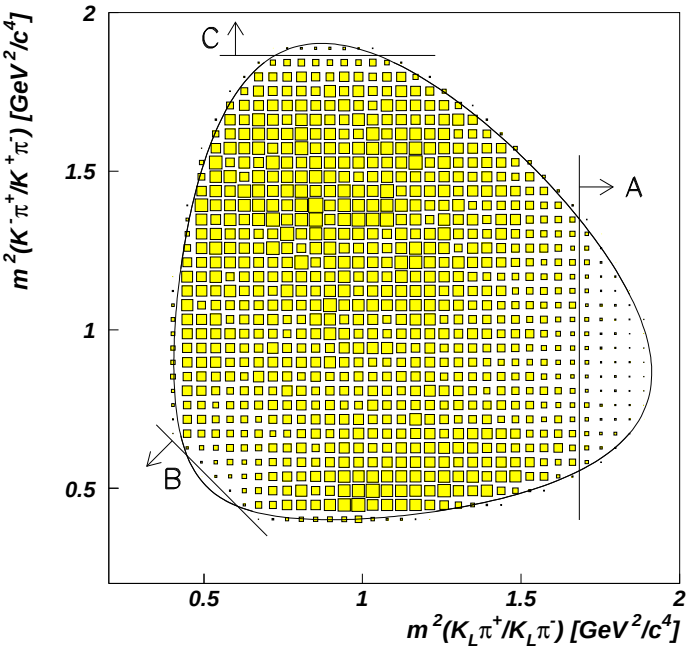

Figure 14: Variation of the acceptance in the $K^{\pm}\pi^{\mp}K_L$ Dalitz plot.

One recognizes a strong decrease in the population in region A of the Dalitz plot. Here the charged kaons are slow enough ($p(K) < 200\,\mathrm{MeV}/c$) to decay within the JDC into $\mu^{\pm}\nu$. This introduces a kink into the track. The reconstruction software resolves the structure into two particles. Therefore, our selection rejects

these kind of events. In region B one looses events with slow pions ($p(\pi) < 50\,\mathrm{MeV}/c$) which cannot reach the crystals (they are bended back into the JDC by the magnetic field). In fig. 15 the lines of constant acceptance for non-interacting K_L are shown. It decreases for increasing K_L momentum and causes the drop in region C of the Dalitz plot fig. 14.

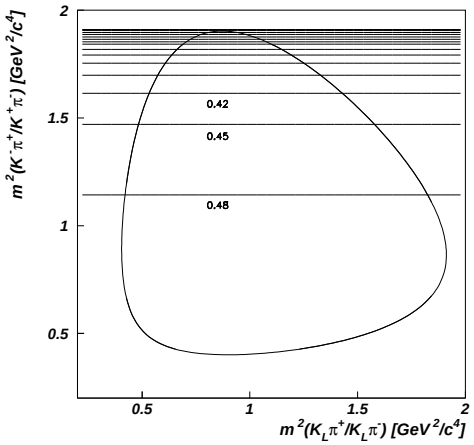

Figure 15: Lines of constant acceptance for the K_L in the $\mathrm{K}^{\pm}\pi^{\mp}\mathrm{K}_L$ Dalitz plot in intervals of 0.03 [7].

The acceptance over the Dalitz plot is formulated as relative deviation from 1 smoothed over phase space. It is

$$\epsilon_i = N_i \cdot \frac{N_{bin}}{\sum_{j=1}^{N_{bin}} N_j} \tag{14}$$

ϵ_i	relative acceptance of cell i
N_i	number of MC-events in cell i
N_{bin}	total number of cells filled.

The number of measured events in each Dalitz plot cell will be corrected by the factor $c_i = 1/\epsilon_i$.

Events with both charged particles having a momentum higher than $450\,\mathrm{MeV}/c$ may be ambiguously identified. This is region A in fig. 16. Misidentified $\mathrm{K}^{\pm}\pi^{\mp}\mathrm{K}_L$ events are reflected with respect to the dashed line. Therefore, they do not leave region A. In region B / C of this plot the pion / kaon has a momentum below $450\,\mathrm{MeV}/c$. In region D both charged particles have a momentum less than $450\,\mathrm{MeV}/c$. The evaluation of the Monte Carlo data reveals a misidentification rate of $(0.75 \pm 0.05)\%$ of all events.

5.3 Acceptance correction for K_L interacting

An interacting K_L can hide in a crystal cluster belonging to charged pions or kaons. For this effect an enhanced probability exsists at the $\bar{\mathrm{K}}\mathrm{K}$ threshold - here

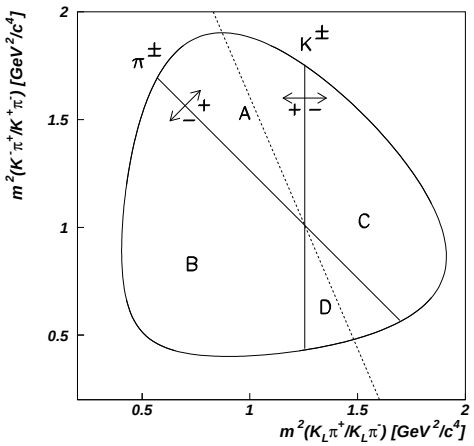

Figure 16: Partition of the Dalitz plot into regions of different momenta for the charged particles. The solid lines correspond to momenta of 450 MeV/c.

both kaon momenta are parallel - and in the region, where the charged pion is parallel to the K_L. The concerned areas are displayed hatched in fig. 17.

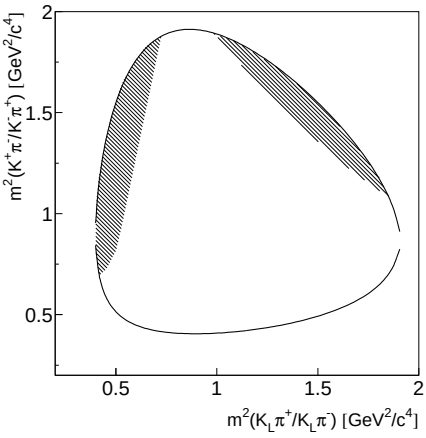

Figure 17: Dalitz plot regions of enhanced probability for a hidden interacting K_L (marked in hatched style).

The effect should be reproduced by the Monte Carlo, at least above a K_L momentum higher than 230 MeV/c (below that value the GEANT [8] output is not reliable). The systematics of the topology of interacting K_L was checked with the annihilation channel $K_L K_S \pi^0$ with $K_S \to \pi^+\pi^-$, which was enhanced by a trigger based on the silicon vertex detector (July'95 data). In this annihilation channel one has a pure kinematical environment for the study of the momentum dependent behaviour of the K_L in the crystals.

5.3.1 Selection of $K_L K_S \pi^0$

The following selection criteria were applied to these data:

1. two opposite charged tracks and any number of PEDs,
2. each track at least an entry in layer 18 or above,
3. simple secondary vertex fit for the K_S; no downstream annihilation,
4. opening angle between tracks at secondary vertex between 20^o and 160^o,
5. $\pi^+\pi^-$ invariant mass equal K_S,
6. $\gamma\gamma$ invariant mass equal π^0,
7. missing mass $K_S\pi^0$ equal K_L,
8. exactly one π^0(in particular exclude $K_S(\pi^+\pi^-)K_S(\pi^0\pi^0)\pi^0$),
9. K_L not in the direction of the π^+, π^- or that of the decay γ belonging to π^0,
10. invariant $\pi^+\pi^-$ mass in the range between 400 MeV and 600 MeV.

From $3.36 \cdot 10^6$ events on tape we extracted 5323 $K_L K_S \pi^0$ events.

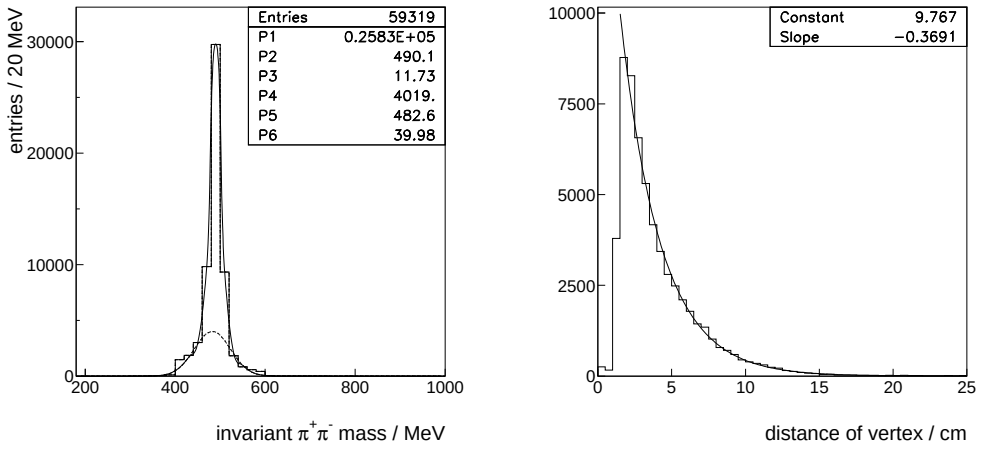

Figure 18: Left: The invariant $\pi^+\pi^-$ mass, fitted to two Gaussian functions. The parameters are given in the box. Right: The K_S vertex distribution, giving the decay length distribution in the labor system (the slope is expected to be -0.37 at a mean K_S momentum of 500 MeV/c).

The invariant $\pi^+\pi^-$ mass and the K_S vertex distribution is shown in fig. 18. Only events with one π^0 plus an arbitrary number of additional PEDs were further considered. The missing mass is shown in fig. 19(left). To determine the direction

of the K_L a kinematic fit was performed, treating the K_L as missing; the additional PEDs have not been considered. Since we only want a sophisticated determination of the K_L direction we do not insist on a good fit quality. The additional PEDs are not allowed to lie in the outer barrel region or in the same cluster as the PEDs already resolved. The K_L - direction is not allowed to match any PED which already belongs to the two charged particles or the π^0.

The number of PEDs after subtraction of the two matched PEDs and the PEDs assigned to the π^0 is displayed in fig. 19(right).

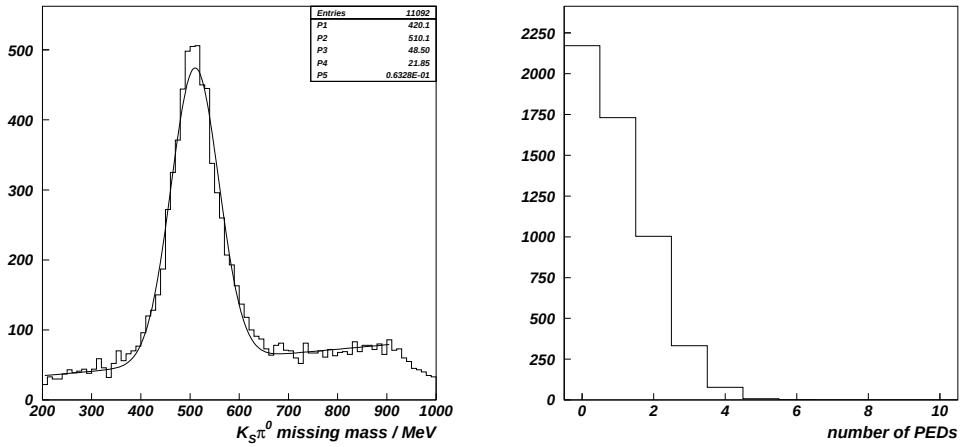

Figure 19: Left: Missing mass $K_S\pi^0$. Right: Number of PEDs (neither assigned to the tracks nor to the γ's of the π^0).

5.3.2 Topology of the K_L PEDs

In the following some characteristics in comparison to the Monte Carlo are presented:

The fig. 20 shows the number of fired crystals grouped to a PED which is assigned to an interacting K_L with momentum greater than 230 MeV/c (dots are data, the line is Monte Carlo). A small deviation is observed at high multiplicities: data PEDs are bigger here.

In fig. 21 the opening angle between the calculated K_L entry in the barrel and the next nearest PED is shown (reference point is the center of the CBAR detector). The expectation is zero degree with some spread. We observe reasonable agreement between data and Monte Carlo. In fig. 22 the angle between the direction of the first nearby PED (see before) and the next nearest PED is shown. Also here one recognizes a compatible description of the spectrum by the Monte Carlo.

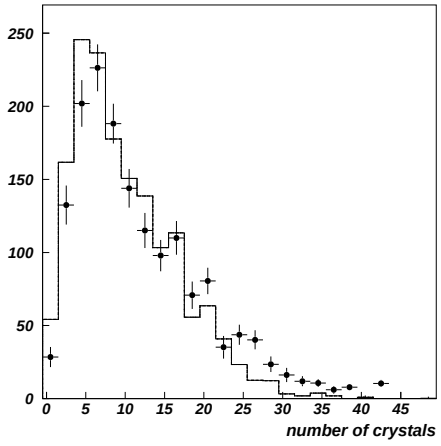

Figure 20: Number of crystals per K_L - PED (dots: data, line: Monte Carlo)

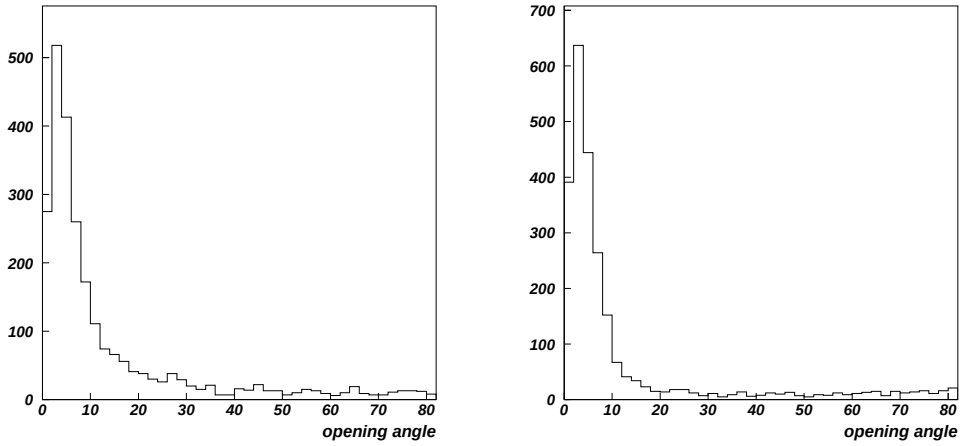

Figure 21: Left: Opening angle between K_L - direction and nearest supernummerary PED (data). Right: Opening angle between K_L direction and nearest supernummerary PED (Monte Carlo).

A more detailed comparison of the topology of the K_L PED was done defining an axis connecting the calculated K_L entry in the crystals and the next nearest PED (see fig. 23). The projections of the crystal positions onto this axis and onto an axis orthotogonal to this one are shown in fig. 24 and fig. 25, respectively. The plots demonstrate, that the Monte Carlo PEDs of an interacting K_L are slightly smaller. The probability, that a hit-crystal cluster of a charged particle and that of a K_L merge is slightly enhanced in data compared to Monte Carlo. The average deviation in the description of the K_L interaction in Monte Carlo versus data is

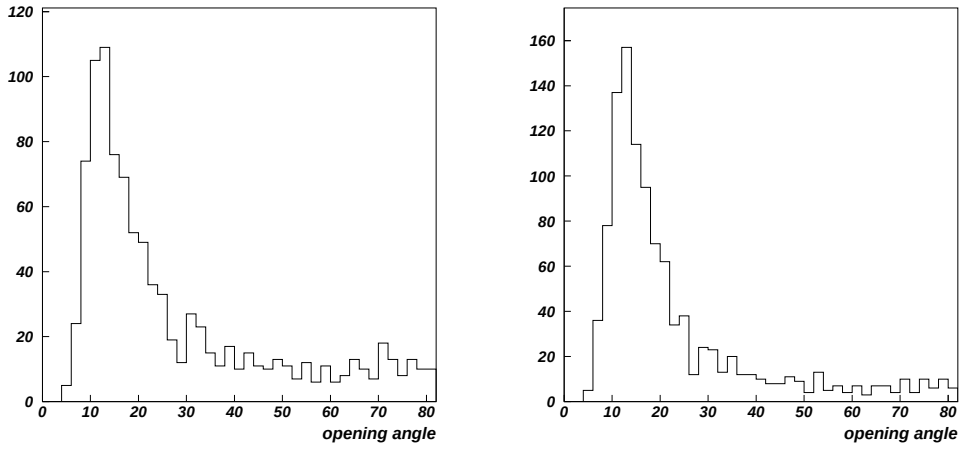

Figure 22: Left: Opening angle between nearest and next nearest supernummerary PED to the K_L - direction (data). Right: Opening angle between nearest and next nearest supernummerary PED to the K_L - direction (Monte Carlo).

taken into account in the acceptance correction (see there).

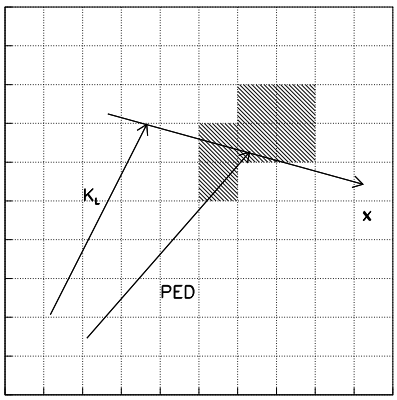

Figure 23: Definition of the K_L direction axis (x). A projection of the hit crystals to this axis (x) and the orthotogonal axis (y) is performed.

5.3.3 K_L(interacting) in the Monte Carlo

We now come to the preparation of the additional acceptance correction for the signal channel. In the first step one has to set a criterium for the identification of an interacting K_L already at the level of the Monte Carlo and before the reconstruction. In order to determine whether a Monte Carlo K_L was interacting in the barrel (interacting in the sense that the CB-offline program will find at least

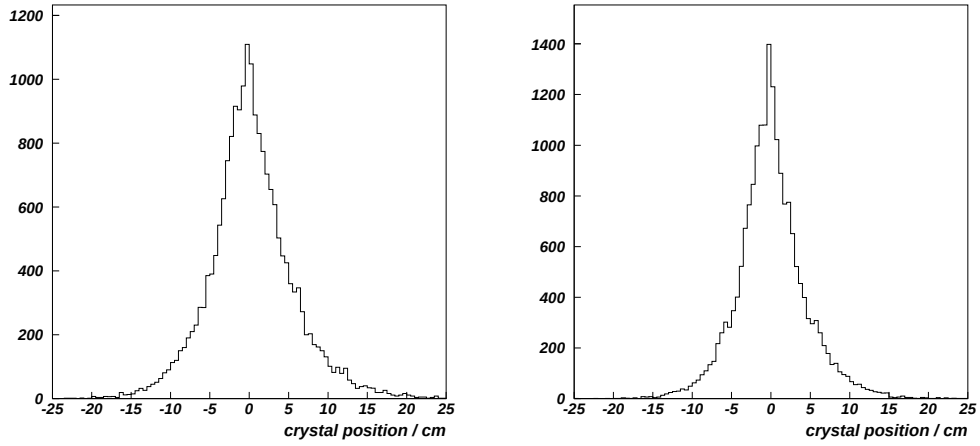

Figure 24: Left: Crystal position (data). Right: Crystal position (Monte Carlo).

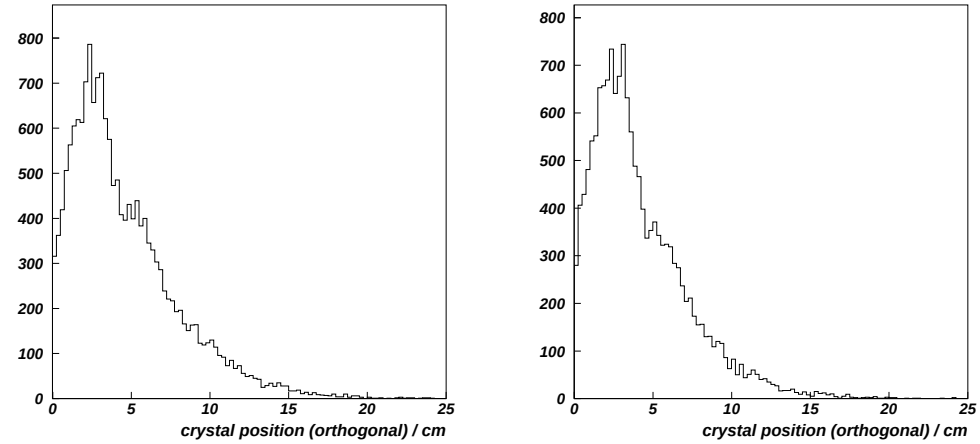

Figure 25: Left: Crystal position orthogonal (data). Right: Crystal position orthogonal (Monte Carlo).

one PED originating from this K_L) a $K_L K^0 \pi^0$ Monte Carlo sample was produced where the K^0 and the π^0 were defined as geantino particles (no interaction whatsoever). In this Monte Carlo every PED found by the reconstruction software has to originate from the K_L. The parameter choosen to tune the Monte Carlo is the maximum energy deposited in a single crystal E^C_{max}. It is accessible from the MC data banks. (solution of the puzzle):

- E^C_{max} : maximum energy deposited by the K_L in a single crystal (values from the Monte Carlo)

The interaction probability is defined via the PED-multiplicity analogous to [7]. Hence, we consider the parameter κ extracted from the Monte Carlo with the offline reconstruction:

$$\kappa(\text{offline}) = \frac{N(PED) > 0}{N(PED) = 0} \tag{15}$$

which has to be equal to

$$\kappa(MC) = \frac{N(E^c_{max} > X)}{N(E^c_{max} < X)} \tag{16}$$

The aim is to find the threshold value X of E^c_{max}, for which the condition $\kappa(\text{offline}) = \kappa(MC)$ is valid. From fig. 26 one reads that a κ of about 1 is achieved at $X = 11$ MeV.

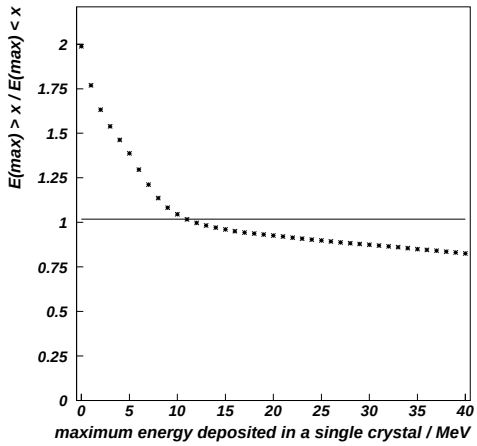

Figure 26: Variation of the ratio κ for E^C_{max} depending on the cutoff parameter X.

Remark: The rough determination of the interaction probability via the described procedure yields a constant value of $P_{int} = 57 \pm 7\%$ for momenta above 230 MeV/c.

5.3.4 Acceptance correction

Using this knowledge, one is able to simulate the full channel $K_L K^+ \pi^-$ and to concentrate on events with interacting K_L flagged by X. The offline reconstruction which demands non-interacting K_L should reject this data sample completely. Due to the hidden K_L this is not the case. Instead one gets the relative acceptance Dalitz plot fig. 27 where the entry A_i in each cell is defined as:

$$A_i = \frac{N^{int}_{rec}}{N^{int}_{gen}}. \tag{17}$$

The total acceptance correction using the momentum dependent interaction probability P_i is calculated the following

$$\epsilon_i = P_i \cdot A_i + (1 - P_i) B_i. \tag{18}$$

Here B_i is the acceptance correction for $K_L K^{\pm}\pi^{\mp}$ with K_L missing as described in section 5.2:

$$B_i = \frac{N_{rec}^{miss}}{N_{gen}^{miss}} \tag{19}$$

After inclusion of the corrections for the K_L interaction one gains the final acceptance correction. In the PWA-fits the acceptance correction due to the K_L hidden effect was varied by plus/minus 5% with no influence to the results.

Correcting the reconstruction efficiency (10) for hidden K_L gives an average reconstruction efficiency of

$$\epsilon_{\mathrm{K}^{\pm}\pi^{\mp}\mathrm{K}_L} = (14.9 \pm 0.1_{stat} \pm 0.5_{syst})\ \%. \tag{20}$$

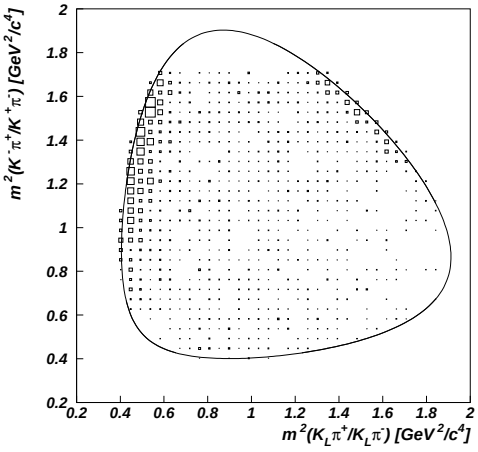

Figure 27: $\mathrm{K}^{\pm}\pi^{\mp}\mathrm{K}_L$ Dalitz plot ($\mathrm{K}^{\pm}\pi^{\mp}\mathrm{K}_L$(interacting), but selection on $\mathrm{K}^{\pm}\pi^{\mp}\mathrm{K}_L$(missing)). There are no events with $p_{K_L} < 230$ MeV/c as the Monte Carlo cross sections are cut off below.

5.4 Branching ratio

As a first order estimate for the number of $\bar{\mathrm{p}}\mathrm{p}$ annihilations $N_{\bar{p}p}$ we use a minimum bias sample of $N_{Minimum\ Bias} = 1{,}066{,}987$ events from the same runperiod June'94. A number of $N_{\mathrm{K}^{\pm}\pi^{\mp}\mathrm{K}_{L(Minimum\ Bias)}} = 213$ events survived the selection cuts. With the reconstruction efficiency of $(14.9 \pm 0.1 \pm 0.5)\%$ one arrives at

the following branching ratio:

$$BR(\mathrm{K}^{\pm}\pi^{\mp}\mathrm{K}_{L(missing)}) = \frac{N_{\mathrm{K}^{\pm}\pi^{\mp}\mathrm{K}_{L}(Minimum\ Bias)}}{N_{Minimum\ Bias} \cdot \epsilon_{\mathrm{K}^{\pm}\pi^{\mp}\mathrm{K}_{L}}} \qquad (21)$$
$$= (1.34 \pm 0.11) \times 10^{-3}.$$

The quoted error is the statistical error only. Not considered here is the trigger-efficiency and the remaining background ((< 5 % ; see section 5.5). With the averaged interaction probability of the K_L in the calorimeter of (54 ± 4) $\times 10^{-2}$ we get:

$$BR(\mathrm{K}^{\pm}\pi^{\mp}\mathrm{K}_{L}) = (2.91 \pm 0.34) \times 10^{-3}. \qquad (22)$$

The value compares well with that of Armenteros et al. [9] for $\mathrm{K}^{\pm}\pi^{\mp}\mathrm{K}_{S}$:

$$BR(\mathrm{K}^{\pm}\pi^{\mp}\mathrm{K}_{S}) = (2.82 \pm 0.11) \times 10^{-3}. \qquad (23)$$

For the estimation of the background the total number of $\bar{\mathrm{p}}\mathrm{p}$ annihilations which lead to the observed number of 11,373 events in the final state $\mathrm{K}^{\pm}\pi^{\mp}\mathrm{K}_{L}$ must be known:

$$N_{\bar{p}p} = \frac{N_{Minimum\ Bias} \cdot N_{\mathrm{K}^{\pm}\pi^{\mp}\mathrm{K}_{L}}}{N_{\mathrm{K}^{\pm}\pi^{\mp}\mathrm{K}_{L}(Minimum\ Bias)}} \cdot \qquad (24)$$
$$= (57.0 \pm 6.0) \times 10^{6}$$

The error contains a systematic uncertainty of about 8% (background ($\approx 4\%$), identification as a $\bar{\mathrm{p}}\mathrm{p}$ annihilation at rest ($\approx 6\%$) [10]).

5.5 Background

Possible background channels, i.e. misidentified events with two tracks without any additional photon found, are:

- $\mathrm{K}^{\pm}\pi^{\mp}\mathrm{K}_{L}$ $\quad \mathrm{K}^{\pm} \rightarrow \mu^{\pm}\nu$
- $\pi^{+}\pi^{-}\pi^{0}$ $\quad$ two γs not seen
- $\pi^{+}\pi^{-}\eta$ $\quad$ two γs not seen
- $\mathrm{K}^{+}\mathrm{K}^{-}\pi^{0}$ $\quad$ two γs not seen
- $\mathrm{K}^{+}\mathrm{K}^{-}$
- $\mathrm{K}_{S}\mathrm{K}_{L}$ $\quad \mathrm{K}_{S} \rightarrow \pi^{+}\pi^{-}$, K_{L} not interacting
- $\pi^{+}\pi^{-}\omega$ $\quad$ three γs not seen
- $\mathrm{K}^{\pm}\pi^{\mp}\mathrm{K}_{L}\pi^{0}$ $\quad \mathrm{K}_{L}$ non-interacting and two γ not seen

The probability to loose two photons is $P_{2\gamma} < 0.2\%$. Background events surviving the selection chain must have at least a high momentum charged particle ($p > 500\,\mathrm{MeV}/c$). Such events are expected at the border of the $\mathrm{K}^{\pm}\pi^{\mp}\mathrm{K}_L$ Dalitz plots.

5.5.1 $\bar{\mathrm{p}}\mathrm{p} \to \mathrm{K}^{\pm}\pi^{\mp}\mathrm{K}_L$, $\mathrm{K}^{\pm} \to \mu^{\pm}\nu$

If the charged kaons are slow enough ($p < 200\,\mathrm{MeV}/c$) they can be stopped within the liquid hydrogen target and decay into $\mu^{\pm}\nu$. The myon possesses a momentum of $235\,\mathrm{MeV}/c$ and is identified as a pion. A fast pion ($p > 500\,\mathrm{MeV}/c$) on the other hand can be misinterpreted as a kaon by the dE/dx. These true $\mathrm{K}^{\pm}\pi^{\mp}\mathrm{K}_L$ events accumulate in a small band as shown in fig. 28. But one expects only 15 ± 4 (0.2%) background events of that type.

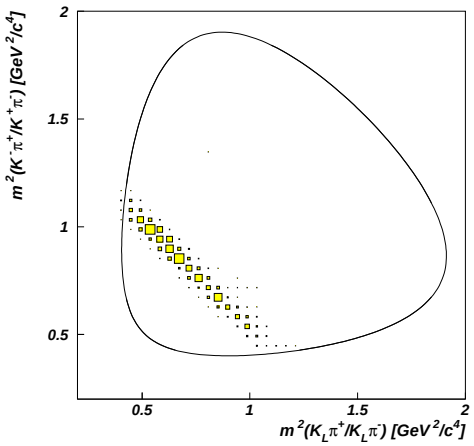

Figure 28: Distribution of $\mathrm{K}^{\pm}\pi^{\mp}\mathrm{K}_L$ events with $\mathrm{K}^{\pm} \to \mu^{\pm}\nu$. Here kaons are confused with pions.

5.5.2 $\bar{\mathrm{p}}\mathrm{p} \to \pi^+\pi^-\pi^0$

This channel is important. Figure 29 shows the $\gamma\gamma$ invariant mass of all PEDs matched by tracks. The shown events have passed the K_L missing mass cut. The described π^0 anti-cut yields a reduction of this background channel by a factor 2.5 . For this channel a weighting with the dynamics in the $\pi^+\pi^-\pi^0$ final state has been performed. According to fig. 30 the background candidates do not originate from regions where events accumulate due to the presence of resonances. In particular they do not come from the $\rho(770)$. In the $\mathrm{K}^{\pm}\pi^{\mp}\mathrm{K}_L$ Dalitz plot these events concentrate on the left edge.

5.5.3 $\bar{\mathrm{p}}\mathrm{p} \to \pi^+\pi^-\eta$

Two photons lost and a fast pion is the signature in that channel, which can produce faked $\mathrm{K}^{\pm}\pi^{\mp}\mathrm{K}_L$ events. These are found in the $\mathrm{K}^{\pm}\pi^{\mp}\mathrm{K}_L$ channel in the

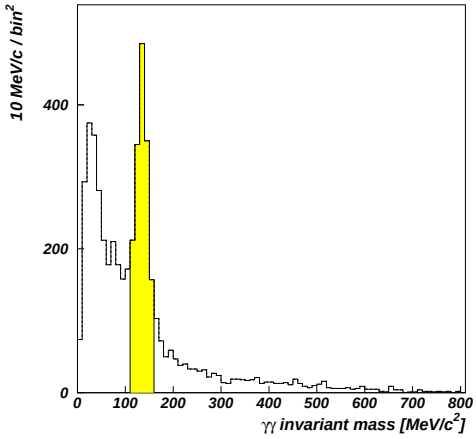

Figure 29: $\gamma\gamma$ invariant mass of all PEDs of $\pi^+\pi^-\pi^0$ Monte Carlo events which passed the K_L missing mass Cut. For most of these events the π^0 decay photons were assigned to the charged tracks.

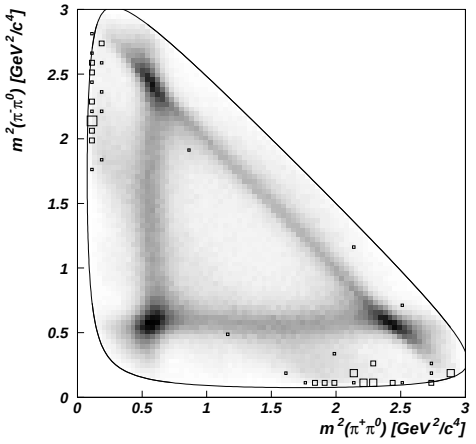

Figure 30: $\pi^+\pi^-\pi^0$ Dalitz plot (698'174 events)[11]. The background $\pi^+\pi^-\pi^0$ Monte Carlo events are superimposed as boxes. The event density corresponds to the size of the boxes.

same region as the $\pi^+\pi^-\pi^0$ background events.

5.5.4 $\bar{p}p \to K^+K^-$

Badly reconstructed K^+K^- events with one fast kaon which is confused with a pion. The marked band A in fig. 32 contains such events with a kaon decaying to $\mu^\pm\nu$. The μ is identified as a pion. The process is very rarely.

5.5.5 $\bar{p}p \to K_SK_L$, $K_S \to \pi^+\pi^-$

As can be seen in fig. 5 K_SK_L events with the K_S decaying into $\pi^-\pi^0$ are kinematically near the $K^\pm\pi^\mp K_L$ events.

Fig. 33 shows the K_SK_L events which survive the preselection and the missing mass cut (exaggerated, to demonstrate): Displayed is the cosine of the opening angle between the two tracks versus the found vertex of the two tracks as calcu-

lated by the reconstruction vertex fit (distance from the target center). There are no events with K_S decaying above a distance of 8 cm because the 2-prong trigger asked for a hit in the inner three layers of the JDC. With the anti-K_S cut 70% of the $K_S K_L$ background can be eliminated.

5.5.6 $\bar{p}p \to K^+K^-\pi^0$

This is the only background contribution found close to the $\bar{K}K$ threshold in $K^\pm\pi^\mp K_L$ (see fig. 35). A fast kaon is mixed with a pion and two photons miss the detection.

5.5.7 $\bar{p}p \to \pi^+\pi^-\omega$

Here three photons must have escaped the detection. The big branching ratio of that channel can compensate the small probability of loosing three photons.

5.5.8 $\bar{p}p \to K^\pm\pi^\mp K_L\pi^0$

To fall into the signal Dalitz plot the K_L must be non-interacting and two photons must be lost. The test using Monte Carlo events showed that the contribution is about 0.2%. It is interesting, that the hypothesis is correctly identified by the dE/dx but the kinematic fit swaps the kaon into a pion and vice versa. Asking for a coincidence in the hypothesis assignement between kinematic fit and dE/dx suppresses this background-channel. The events belonging to that 4-body final state are found in the left corner of the Dalitz plot together with $\pi^+\pi^-\pi^0$.

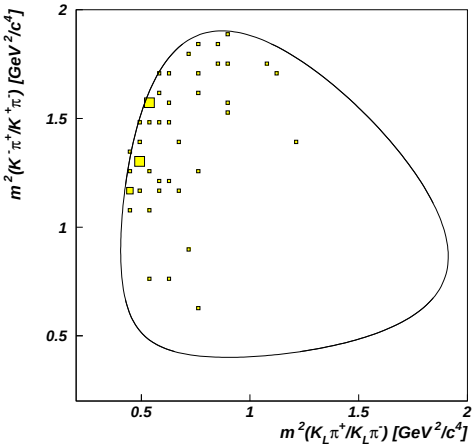

Figure 31: $\pi^+\pi^-\eta$ background in the $K^{\pm}\pi^{\mp}K_L$ Dalitz plot.

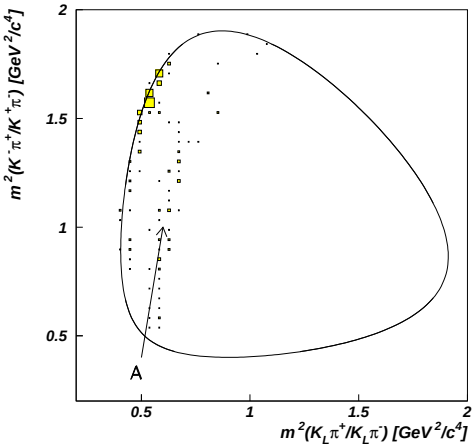

Figure 32: K^+K^- background in the $K^{\pm}\pi^{\mp}K_L$ Dalitzplot.

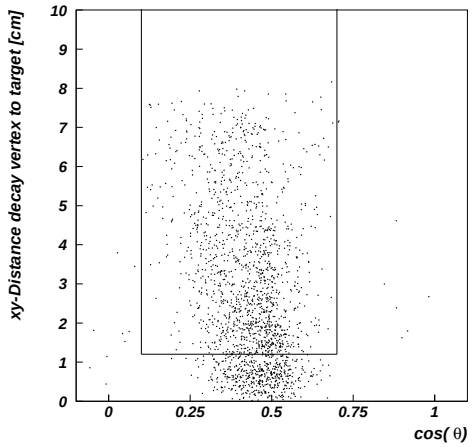

Figure 33: Cosine of the decay angle of the K_S versus the distance of the K_S decay vertex to the target center for K_SK_L Monte Carlo events. Events within the drawn box are rejected.

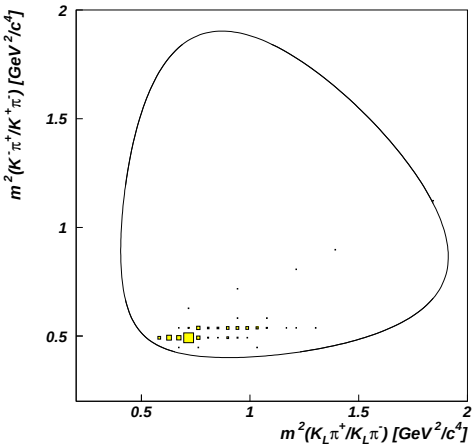

Figure 34: K_SK_L background in the $K^{\pm}\pi^{\mp}K_L$ Dalitz plot.

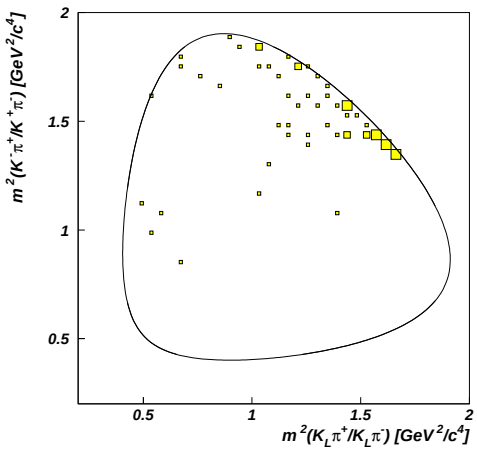

Figure 35: $K^+K^-\pi^0$ background in the $K^\pm\pi^\mp K_L$ Dalitz plot.

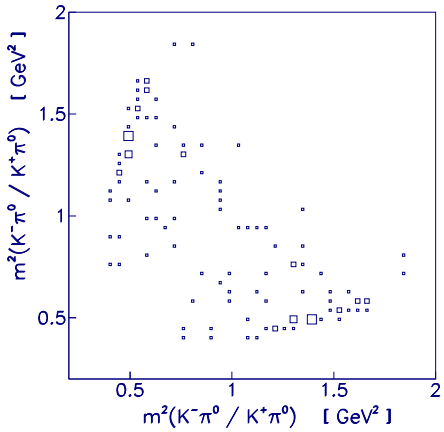

Figure 36: The origin of the $K^+K^-\pi^0$ background in its Dalitz plot.

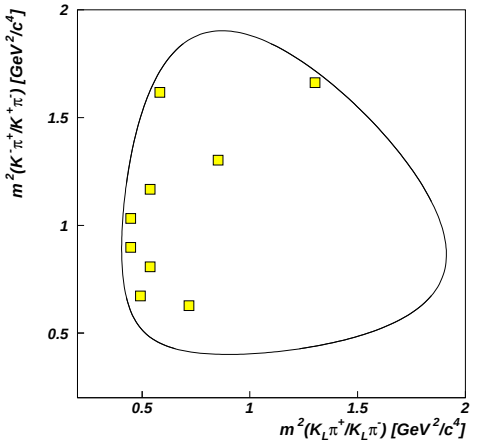

Figure 37: The $\pi^+\pi^-\omega$ background in the $K^\pm\pi^\mp K_L$ Dalitz plot.

5.5.9 Background summary

With the number of produced MC-events per channel N_{MC}, the number of $\bar{\mathrm{p}}\mathrm{p}$ annihilations considered $N_{\overline{p}p}$ (see section 5.4) and the branching ratios BR_{BG} of the background channels collected in table 6 the true number of background events N_{BG}^{eff} in the $\mathrm{K}^{\pm}\pi^{\mp}\mathrm{K}_L$ Dalitz plot is obtained the following:

$$N_{BG}^{eff} = \frac{N_{\overline{p}p} \cdot BR_{BG}}{N_{MC}} \cdot N_{BG} \; . \tag{25}$$

	branching ratios	reference
$\pi^+\pi^-\pi^0$	$(6.6 \pm 0.8) \times 10^{-2}$ †	[12]
$\pi^+\pi^-\eta$	$(1.37 \pm 0.15) \times 10^{-2}$ †	[13]
$\mathrm{K}^+\mathrm{K}^-\pi^0$	$(2.6 \pm 0.6) \times 10^{-3}$	[14]
$\mathrm{K}^+\mathrm{K}^-$	$(0.99 \pm 0.05) \times 10^{-3}$	[10]
$\mathrm{K}_S\mathrm{K}_L$	$(9.07 \pm 0.24) \times 10^{-4}$	[15]
$\pi^+\pi^-\omega$	$(6.6 \pm 0.6) \times 10^{-2}$	[16]

† assuming 100 % annihilation from $\bar{\mathrm{p}}\mathrm{p}$ S-state

Table 6: Applied branching ratios for the background channels in the channel $\bar{\mathrm{p}}\mathrm{p} \to \mathrm{K}^{\pm}\pi^{\mp}\mathrm{K}_L$.

In table 7 the generated and selected background events are summarized. The corresponding background Dalitz plot is shown in fig. 38. The faked events are concentrated at the left border of the Dalitz plot. Some events are found in the upper region of the $\mathrm{a}_0(980)$. The small number of remaining $\mathrm{K}_S\mathrm{K}_L$ events is seen as a faint band in the lower part. In the reconstructed $\mathrm{K}^{\pm}\pi^{\mp}\mathrm{K}_L$ channel one expects 190 ± 22 background events. The systematic error of this number is established by varying the parameters M and N of the dE/dx calibration (see section 4.6) within their error range. This leads to the fraction of $(1.7^{+\,1.7}_{-\,0.7})$ % of background events.

6 The Dalitz plot

Now we can present the $\mathrm{K}^{\pm}\pi^{\mp}\mathrm{K}_L$ Dalitz plot of the June'94 data, acceptance corrected and background subtracted. It is shown in fig. 39 together with the projections into the subsystems $\mathrm{K}_L\pi^{\pm}$ fig. 40, $\mathrm{K}^{\pm}\pi^{\mp}$ fig. 41 and $\mathrm{K}_L\mathrm{K}^{\pm}$ fig. 42.

The Dalitz plot is asymmetric since we have plotted the neutral versus the charged $K\pi$ system. The asymmetry is due to the different interferences of the

channel		generated events	selected events	bgd. normalized to $N_{\bar{p}p}$
$\pi^+\pi^-\pi^0$ phase space		1'600'000	59	139 ± 29
$\pi^+\pi^-\pi^0$ weighted		1'600'000	25	60 ± 16
$\pi^+\pi^-\eta$,	$\eta \to \gamma\gamma$	300'000	46	47 ± 10
$K^+K^-\pi^0$		300'000	57	28 ± 9
K^+K^-		300'000	141	27 ± 4
K_SK_L,	$K_S \to \pi^+\pi^-$	100'000	102	18 ± 3
$\pi^+\pi^-\omega$,	$\omega \to \pi^0\gamma$	300'000	9	10 ± 4
Total ($\pi^+\pi^-\pi^0$ weighted)				190 ± 22

Table 7: Background in the $K^{\pm}\pi^{\mp}K_L$ channel.

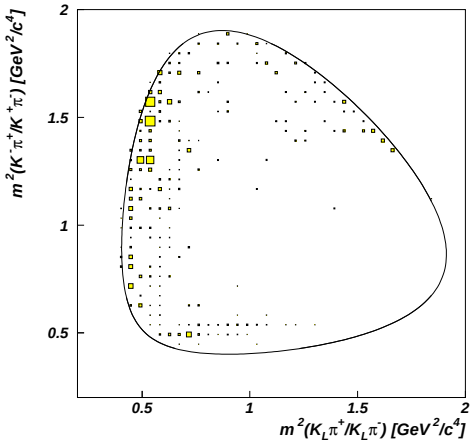

Figure 38: Sum of the background channels, each normalized according to its branching ratio.

resonances coming from the isospin $I = 0$ and $I = 1$ initial state. The first order features which easily can be identified by eye are the $a_0(980)$ at the $\bar{K}K$ threshold and the $a_2(1320)$, which appears along the diagonal and preferentially at the boundaries. Other dominant structures in the $K\pi$ systems are the two $K^*(892)$ bands interfering destructively in the lower part of the Dalitz plot. The interference between the $a_2(1320)$ and the K^* causes a deviation from a straight line for the K^* resonance band. Between the K^* bands and the $a_2(1320)$ one

observes reduced population. On the other hand below the K^{*0} band along the diagonal one sees additional intensity (corresponds to about 1500 MeV/c^2). We will see, that this behaviour is described by the scalar $\bar{\mathrm{K}}$K resonance $a_0(1450)$. In addition the small bump appearing at the end of the $K^{*\pm}$ band will partly be explained by an additional $\bar{\mathrm{K}}$K vector resonance.

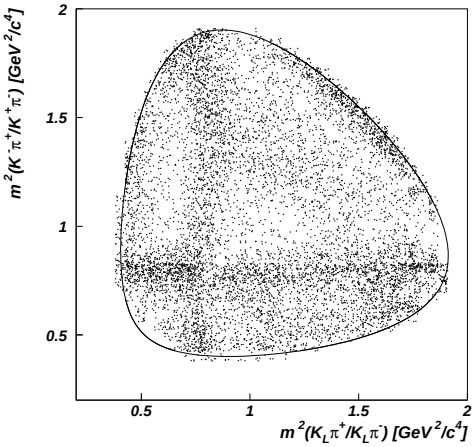

Figure 39: Acceptance corrected $K^{\pm}\pi^{\mp}K_L$ Dalitz plot (background subtracted).

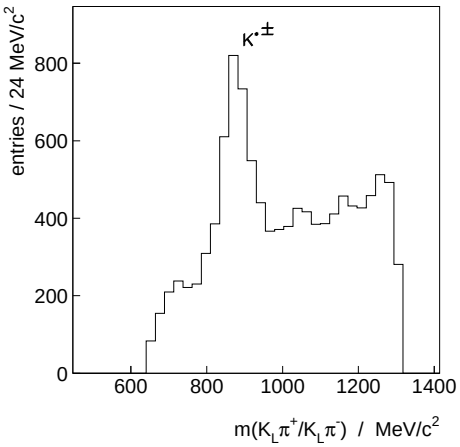

Figure 40: Projection of the acceptance corrected $K^{\pm}\pi^{\mp}K_L$ Dalitz plot into the $K_L\pi^{\pm}$ subsystem.

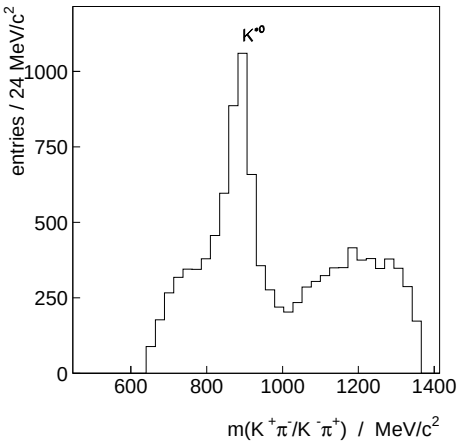

Figure 41: Projection of the acceptance corrected $K^{\pm}\pi^{\mp}K_L$ Dalitz plot into the $K^{\pm}\pi^{\mp}$ subsystem.

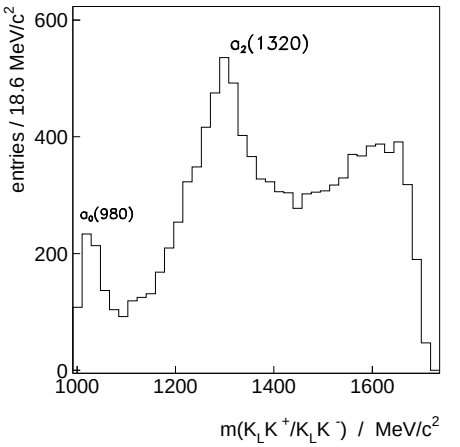

Figure 42: Projection of the acceptance corrected $K^{\pm}\pi^{\mp}K_L$ Dalitz plot into the $K_LK^{\pm}$ subsystem.

7 Partial wave analysis

The partial wave analysis (PWA) will be performed as a χ^2 test of the theoretical Dalitz plot density compared to the event density.

7.1 Transition amplitude

The transition amplitude is formulated in the frame of the isobar model: the transition from a certain $\bar{\mathrm{p}}\mathrm{p}$ initial state to the three body final state proceeds via intermediate two body resonances (isobars). In principle, this needs no further explanation, since the model [17] and the way the dynamical part of the amplitude is formulated in the K-matrix formalism [18] should be well known to the reader. The total amplitude can be written as a product of a dynamical amplitude and a spin-parity function. In addition one has to take care of the summation for different isospin transitions (weighted by Clebsch Gordan coefficients) and the symmetrization for identical particles in the final state.

The general transition amplitude from a $\bar{\mathrm{p}}\mathrm{p}$ initial state $I^G(J^{PC})$ to a three body final state via a two-body resonance with spin l evaluated at a Dalitz plot position (m_{12}^2, m_{13}^2) is given as:

$$A_f = A_{J^{PC}}(m_{12}^2, m_{13}^2) = \sum_{I_3} f_{l,L,I_3}(m_{12}^2, m_{13}^2) \cdot \widehat{F}_{l,I_3}(m_{12}^2, m_{13}^2) \cdot C_{I,I_3} \tag{26}$$

$f_{I,I_3}(m_{12}^2, m_{13}^2)$	spin-parity function
$\widehat{F}_{I,I_3}(m_{12}^2, m_{13}^2)$	dynamical function
C_{I,I_3}	isospin dependence: it is a product of Clebsch-Gordan coefficients in dependence of the isospin of the initial state and that of the participating particles (see below).

In $\bar{\mathrm{p}}\mathrm{p}$ annihilation at rest all transitions from a certain $I^G(J^{PC})$ initial state add coherently. The different $\bar{\mathrm{p}}\mathrm{p}$ initial states do not interfere. The intensity in a Dalitz plot cell $\mathcal{I}((m_{12}^2, m_{13}^2)$ with border lengths Δm_{12}^2 and Δm_{13}^2 at the position (m_{12}^2, m_{13}^2) is calculated by integration over the phase space density:

$$\begin{aligned}
\mathcal{I}(m_{12}^2, m_{13}^2) &= \int_{\Delta m_{12}^2} \int_{\Delta m_{13}^2} I(m_{12}^2, m_{13}^2) dm_{12}^2 dm_{13}^2 \\
&= \int_{\Delta m_{12}^2} \int_{\Delta m_{13}^2} \sum_{J^{PC}} I_{J^{PC}}(m_{12}^2, m_{13}^2) dm_{12}^2 dm_{13}^2 \\
&= N_{PS} \cdot \int_{\Delta m_{12}^2} \int_{\Delta m_{13}^2} \sum_{J^{PC}} \left| \sum_{f_j=1}^{n_j} \xi_{f_j} e^{i\Phi_{f_j f_j'}} A_{f_j}(m_{12}^2, m_{13}^2) \right|^2 dm_{12}^2 dm_{13}^2 \ ,
\end{aligned} \tag{27}$$

where $N_{PS} = \frac{\pi^2}{4(2m_p)^2}$.

ξ_f	relative strength of the transition
$\Phi_{ff'}$	relative phase between different transitions from one initial state. Since an absolute phase can not be determined, one sets $\Phi_{12} = 0$.

7.1.1 Spin-parity function

Angular momenta and the decay angle are defined in the Jackson frame according to fig. 43.

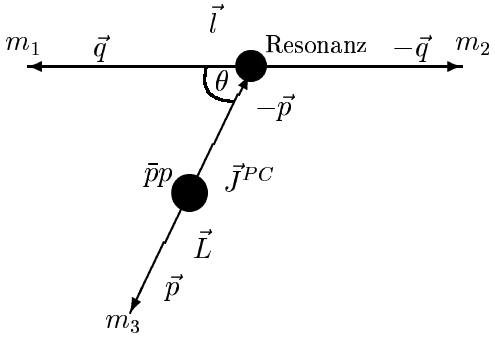

Figure 43: The Gottfried-Jackson system: definition of the kinematics.

$(m_1, m_2), m_3$	:	masses of the final state particles
$\vec{p}$	:	momentum of the primary decay
$\vec{q}$	:	decay momentum of the isobar
J^{PC}	:	spin-parity of the initial state
L	:	angular momentum between resonance and spectator meson
l	:	spin of the di-meson

For the decay into three pseudoscalar mesons the amplitude can be formulated either in the helicity formalism (for $\bar{\text{p}}$p annihilation at rest one has to integrate over the production angles, since the initial state is not polarized) or the Zemach formalism.

7.1.2 Dynamical function

According to Jackson [20] the cross section of $\bar{\mathrm{p}}\mathrm{p}$ decay into three particles is dominated by the two-body scattering between two of them. The third particle acts as spectator of the process. The dynamical function $\widehat{F}$ a priori is a two-body scattering amplitude, where the coupling Γ_i to the initial state is replaced by the production strength ξ_i in $\bar{\mathrm{p}}\mathrm{p}$ annihilation at rest. In the simplest case with no resonant scattering $\widehat{F}$ is just a constant. In general the $\widehat{F}$ function can be derived from the formulation of 2-body scattering in the K-matrix formalism [18].

7.1.3 Centrifugal barrier

For the centrifugal barrier we have choosen the Blatt-Weisskopf factors [19], so far applied in all our Dalitzplot analyses.

7.1.4 Isospin decomposition

Now we come to a rather expensive consideration.

$K\pi$ system

Isospin decomposition of $\bar{\mathrm{p}}\mathrm{p} \to \pi\bar{\mathrm{K}}\mathrm{K}$ for the coupling of $K\pi$ to K^* with $I = 1/2$. Definition of the isospin dublets of the kaons:

$$\begin{pmatrix} K^+ \\ K^0 \end{pmatrix} \quad \begin{pmatrix} \overline{K}^0 \\ -K^- \end{pmatrix} \quad \begin{matrix} i_3 = \frac{1}{2} \\ i_3 = -\frac{1}{2}. \end{matrix} \tag{28}$$

The wave function is a superposition of all charge combinations with couplings given by the Clebsch-Gordan coefficients $\langle J\,M|j_1\,j_2\,m_1\,m_2\rangle$ (with the kaon-definition above the Clebsch-Gordan coefficients for the K^- and K^{*-} get an additional minus sign).

- $|K^{*+}\rangle = \alpha|K^+\pi^0\rangle + \beta|K^0\pi^+\rangle$
  $\alpha = \langle\frac{1}{2}\,\frac{1}{2}|\frac{1}{2}\,1\,\frac{1}{2}\,0\rangle = +\sqrt{1/3}$
  $\beta = \langle\frac{1}{2}\,\frac{1}{2}|\frac{1}{2}\,1\,-\frac{1}{2}\,1\rangle = -\sqrt{2/3}$

$$|K^{*+}\rangle \;=\; \frac{1}{\sqrt{3}}(|K^+\pi^0\rangle - \sqrt{2}|K^0\pi^+\rangle), \tag{29}$$

- $|K^{*-}\rangle = \alpha|K^-\pi^0\rangle + \beta|\overline{K}^0\pi^-\rangle$
  $\alpha = \langle\frac{1}{2}\,-\frac{1}{2}|\frac{1}{2}\,1\,-\frac{1}{2}\,0\rangle = -\sqrt{1/3}$

$\beta = \langle \frac{1}{2}\ -\frac{1}{2} | \frac{1}{2}\, 1\, \frac{1}{2}\ -1 \rangle = -\sqrt{2/3}$

$$|K^{*-}\rangle = \frac{1}{\sqrt{3}}(-|K^-\pi^0\rangle - \sqrt{2}|\overline{K}^0\pi^-\rangle), \tag{30}$$

- $|K^{*0}\rangle = \alpha|K^+\pi^-\rangle + \beta|K^0\pi^0\rangle$
  $\alpha = \langle \frac{1}{2}\ -\frac{1}{2} | \frac{1}{2}\, 1\, \frac{1}{2}\ -1 \rangle = +\sqrt{2/3}$
  $\beta = \langle \frac{1}{2}\ -\frac{1}{2} | \frac{1}{2}\, 1\ -\frac{1}{2}\, 0 \rangle = -\sqrt{1/3}$

$$|K^{*0}\rangle = \frac{1}{\sqrt{3}}(\sqrt{2}|K^+\pi^-\rangle - |K^0\pi^0\rangle), \tag{31}$$

- $|\overline{K}^{*0}\rangle = \alpha|K^-\pi^+\rangle + \beta|\overline{K}^0\pi^0\rangle$
  $\alpha = \langle \frac{1}{2}\ \frac{1}{2} | \frac{1}{2}\, 1\ -\frac{1}{2}\, 1 \rangle = +\sqrt{2/3}$
  $\beta = \langle \frac{1}{2}\ \frac{1}{2} | \frac{1}{2}\, 1\ \frac{1}{2}\, 0 \rangle = +\sqrt{1/3}$

$$|\overline{K}^{*0}\rangle \ = \ \frac{1}{\sqrt{3}}(\sqrt{2}|K^-\pi^+\rangle + |\overline{K}^0\pi^0\rangle). \tag{32}$$

Now one has to calculate the couplings to the intermediate states $K^*\overline{K}$ and $\overline{K}^*K$ with $I = 0$ or $I = 1$. For $\bar{\mathrm{p}}\mathrm{p}$ annihilation at rest we have to consider $i_3 = 0$ only.

- $|K^*\overline{K}\rangle_I = \alpha|K^{*+}K^-\rangle_I + \beta|K^{*0}\overline{K}^0\rangle_I$
  $I = 0$: $\alpha = \langle 0\,0 | \frac{1}{2}\ \frac{1}{2}\ \frac{1}{2}\ -\frac{1}{2} \rangle = -\sqrt{1/2}$
  $\beta = \langle 0\,0 | \frac{1}{2}\ \frac{1}{2}\ -\frac{1}{2}\ \frac{1}{2} \rangle = -\sqrt{1/2}$

  $I = 1$: $\alpha = \langle 1\,0 | \frac{1}{2}\ \frac{1}{2}\ \frac{1}{2}\ -\frac{1}{2} \rangle = -\sqrt{1/2}$
  $\beta = \langle 1\,0 | \frac{1}{2}\ \frac{1}{2}\ -\frac{1}{2}\ \frac{1}{2} \rangle = +\sqrt{1/2}$

$$|K^*\overline{K}\rangle_I \ = \ \frac{1}{\sqrt{2}}(-|K^{*+}K^-\rangle_I + (-1)^{I+1}|K^{*0}\overline{K}^0\rangle_I), \tag{33}$$

- $|\overline{K}^*K\rangle_I = \alpha|K^{*-}K^+\rangle_I + \beta|\overline{K}^{*0}K^0\rangle_I$

$$
\begin{aligned}
I=0: \quad \alpha &= \langle 0\,0|\tfrac{1}{2}\,\tfrac{1}{2}\,-\tfrac{1}{2}\,\tfrac{1}{2}\rangle = +\sqrt{1/2} \\
\beta &= \langle 0\,0|\tfrac{1}{2}\,\tfrac{1}{2}\,\tfrac{1}{2}\,-\tfrac{1}{2}\rangle = +\sqrt{1/2}
\end{aligned}
$$

$$
\begin{aligned}
I=1: \quad \alpha &= \langle 1\,0|\tfrac{1}{2}\,\tfrac{1}{2}\,-\tfrac{1}{2}\,\tfrac{1}{2}\rangle = -\sqrt{1/2} \\
\beta &= \langle 1\,0|\tfrac{1}{2}\,\tfrac{1}{2}\,\tfrac{1}{2}\,-\tfrac{1}{2}\rangle = +\sqrt{1/2}
\end{aligned}
$$

$$
|\overline{K}^* K\rangle_I \;=\; \frac{1}{\sqrt{2}}((-1)^I |K^{*-}K^+\rangle_I + |\overline{K}^{*0}K^0\rangle_I). \tag{34}
$$

With the defined C-parity of the $\bar{\mathrm{p}}\mathrm{p}$ initial state, one has to take into account

$$
\begin{aligned}
\mathbf{C}|K^{*0}\overline{K}^0\rangle &= -|\overline{K}^{*0}K^0\rangle \\
\mathbf{C}|K^{*+}K^-\rangle &= -|K^{*-}K^+\rangle
\end{aligned} \tag{35}
$$

and the decomposition above (33) together with (34) for isospin $I=0$ or $I=1$ one gets:

$$
\begin{aligned}
\mathbf{C}|K^*\overline{K}\rangle_{I=0} &= +|\overline{K}^* K\rangle_{I=0} \\
\mathbf{C}|K^*\overline{K}\rangle_{I=1} &= -|\overline{K}^* K\rangle_{I=1}\,.
\end{aligned} \tag{36}
$$

Hence, with $I_{K^*}=1/2$, $I=I_{K^*K}=I_{\overline{p}p}=0,1$ and $C=\pm 1$ the eigenstates $\Phi^C_{I,I_{K^*}}$ are:

$$
\begin{aligned}
\Phi^C_{0,\frac{1}{2}} &= \frac{1}{\sqrt{2}}\,(|K^*\overline{K}\rangle_{I=0} + C|\overline{K}^* K\rangle_{I=0}) \\
&= \frac{1}{\sqrt{12}}\left\{\begin{array}{c} -|K^+\pi^0 K^-\rangle + \sqrt{2}|K^0\pi^+ K^-\rangle \\ -\sqrt{2}|K^+\pi^-\overline{K}^0\rangle + |K^0\pi^0\overline{K}^0\rangle \\ +C[-|K^-\pi^0 K^+\rangle - \sqrt{2}|\overline{K}^0\pi^- K^+\rangle \\ +\sqrt{2}|K^-\pi^+ K^0\rangle + |\overline{K}^0\pi^0 K^0\rangle] \end{array}\right\}
\end{aligned} \tag{37}
$$

and

$$
\begin{aligned}
\Phi^C_{1,\frac{1}{2}} &= \frac{1}{\sqrt{2}}\,(|K^*\overline{K}\rangle_{I=1} - C|\overline{K}^* K\rangle_{I=1}) \\
&= \frac{1}{\sqrt{12}}\left\{\begin{array}{c} -|K^+\pi^0 K^-\rangle + \sqrt{2}|K^0\pi^+ K^-\rangle \\ +\sqrt{2}|K^+\pi^-\overline{K}^0\rangle - |K^0\pi^0\overline{K}^0\rangle \\ +C[-|K^-\pi^0 K^+\rangle - \sqrt{2}|\overline{K}^0\pi^- K^+\rangle \\ -\sqrt{2}|K^-\pi^+ K^0\rangle - |\overline{K}^0\pi^0 K^0\rangle] \end{array}\right\}.
\end{aligned} \tag{38}
$$

The same way one derives for $I_{K^*} = 3/2$ and $I = I_{K^*K} = I_{\overline{p}p} = 1$:

$$\Phi^C_{1,\frac{3}{2}} = \frac{1}{\sqrt{12}} \left\{ \begin{array}{r} -\sqrt{2}|K^+\pi^0K^-\rangle - |K^0\pi^+K^-\rangle \\ -|K^+\pi^-\overline{K}^0\rangle - \sqrt{2}|K^0\pi^0\overline{K}^0\rangle \\ +C[-\sqrt{2}|K^-\pi^0K^+\rangle + |\overline{K}^0\pi^-K^+\rangle \\ +|K^-\pi^+K^0\rangle - \sqrt{2}|\overline{K}^0\pi^0K^0\rangle)] \end{array} \right\}. \tag{39}$$

In general, the $\pi K\overline{K}$ final state is symmetrical under the exchange of kaons, if the G-parity of the $\bar{\mathrm{p}}\mathrm{p}$ system is $G = (-1)^I C = +1$ and anti-symmetrical for $G = -1$. In consequence one has:

- constructive interference between $K^*\overline{K}$ and $\overline{K}^*K$ amplitudes for $I_{\overline{p}p} = 0$,
- destructive interference between $K^*\overline{K}$ and $\overline{K}^*K$ amplitudes for $I_{\overline{p}p} = 1$.

Then, the relative phase between the two amplitudes is $\phi = 0°$ and $\phi = 180°$, respectively.

$\bar{\mathrm{K}}\mathrm{K}$ system

The isospin decomposition of $\pi K\overline{K}$ can also be made with respect to the $\bar{\mathrm{K}}\mathrm{K}$ coupling. With $I_{K\overline{K}}$ being the isospin of the $K\overline{K}$ system and $C = \pm 1$ the C-parity eigenstates $\Psi^C_{I,I_{K\overline{K}}}$ are given as:

$$\Psi^C_{0,1} = -\frac{1}{\sqrt{12}} \left\{ \begin{array}{c} -|\pi^0K^+K^-\rangle + |\pi^0K^0\overline{K}^0\rangle \\ +\sqrt{2}|\pi^+K^0K^-\rangle - \sqrt{2}|\pi^-K^+\overline{K}^0\rangle \\ +C[-|\pi^0K^-K^+\rangle + |\pi^0\overline{K}^0K^0\rangle \\ -\sqrt{2}|\pi^-\overline{K}^0K^+\rangle + \sqrt{2}|\pi^+K^-K^0\rangle] \end{array} \right\}, \tag{40}$$

$$\Psi^C_{1,0} = \frac{1}{2} \left\{ \begin{array}{c} -|\pi^0K^+K^-\rangle - |\pi^0K^0\overline{K}^0\rangle \\ +C[-|\pi^0K^-K^+\rangle - |\pi^0\overline{K}^0K^0\rangle] \end{array} \right\}, \tag{41}$$

$$\Psi^C_{1,1} = \frac{1}{2} \left\{ \begin{array}{c} -|\pi^+K^0K^-\rangle - |\pi^-K^+\overline{K}^0\rangle \\ +C[|\pi^-\overline{K}^0K^+\rangle + |\pi^+K^-K^0\rangle] \end{array} \right\}. \tag{42}$$

7.2 Fit - Procedure

The data Dalitz plot was prepared the following before it went into the fit:

- background was subtracted according to sec. 5.5
- remaining events were acceptance corrected according to sec. 5.3

- the binning: 0.045 GeV^2/c^4 $\times$ 0.045 GeV^2/c^4
- cells at the Dalitz plot border were rejected (at least if the cell area within the boundary was less than 30%)

For the partial wave analysis 730 cells could be used after application of the criteria above.

The test of the different hypotheses was done using the program COPWA [21] which is in particular designed to handle 3-body final states. It is based on the standard CERN-software MINUIT [22]. A maximum likelihood method for a binned data sample was used. The quantity to be minimized is formulated as an equivalent chisquare according to [23]. (just for comparison we will mention the values of the (least squares) chisquares applied usually, the Neyman (error calculated from data) and Pearson (error calculated from theory) quantities.) Assuming a Poisson statistics for the number of events per Dalitz plot bin one arrives at the Poisson likelihood chisquare [23] :

$$\chi^2_L = 2 \sum_i y_i - n_i + n_i \ln(n_i/y_i), \tag{43}$$

where n_i is the number of events in the i-th bin and y_i is the number of events predicted by the model in the i-th bin. It is calculated at various positions within a cell. The following χ^2 function is the well known Neyman quantity:

$$\chi^2 = \sum_{j=1}^{N_{Zellen}} \frac{(n_j - y_j)^2}{\sigma_j^2(n_j) + \sigma_{j\,syst}^2)} \; . \tag{44}$$

n_j is the number of measured events per cell j after subtraction of the background and after acceptance correction (and after correction of the area of the cells which are only partly within the Dalitz plot):

$$n_j = (N_j - B_j) \cdot c_j \; . \tag{45}$$

Here N_j is the number of events in the $K^{\pm}\pi^{\mp}K_L$ Dalitz plot in cell j ($N_j > 2$), B_j the number of background events in the corresponding cell j and c_j the acceptance correction. The error is given by:

$$\sigma_j^2(n_j) = (N_j + B_j) \cdot c_j^2 \tag{46}$$

The error belonging to the K_L interaction probability was neglected but the influence of the correction is checked by its variation during the fit.

Each partial wave is normalized individually by integration over the full phase space. The content of each resonance is extracted by its integration over phase space in one subsystem of the Dalitz plot, setting the production strengths of all other contributive resonances to zero. In consequence, for strongly overlapping resonances in a partial wave or strong interferences between different partial waves the individual intensities may not sum up to 100%.

7.3 Partial waves

In the following the generics of the partial waves tested will be shown. It will allow the reader to estimate by eye what the data Dalitz plot may be composed of. But the simulations contain no interference informations. The initial states considered are ^{1}S$_0$ and ^{3}S$_1$, according to the knowledge [25, 26] that $\bar{\text{p}}$p annihilation in liquid hydrogen is dominated be S-states. As a check, once having a final description of the K$^\pm\pi^\mp$K$_L$ final state, we will allow for P-states in addition. Without explicit knowledge, one can perform an iterative adoption of the P-state transitions until they reach the expected intensity.

initial state $^{(2S+1)}L_J$	J^{PC}	resonance		anngular distribution
$^1S_0$	0^{-+}	K_0^* (1430)	K	1
		$K^*(892)$	K	$\cos^2\theta$
		a$_0$(980)+ a_0(1450)	π	1
		$\rho(1450)+\rho(1700)$	π	$\cos^2\theta$
		a$_2$(1320)	π	$(\cos^2\theta-\frac{1}{3})^2$
$^3S_1$	1^{--}	$K^*(892)$	K	$\sin^2\theta$
		$\rho(1450)+\rho(1700)$	π	$\sin^2\theta$
		a$_2$(1320)	π	$\sin^2\theta\cos^2\theta$

Table 8: Angular distributions of considered resonances.

- $\bar{\text{p}}\text{p}\ (^1\text{S}_0) \to K^*(892)K$, $K^*(892) \to K\pi$ (fig. 44 fig. 45)

  The K^* decays into $K\pi$ with a relative angular momentum of 1 (relative P-wave). The angular momentum of the recoiling K is $L = 1$. It is the only relevant resonance in the P-wave and therefore parametrized as a Breit-Wigner amplitude. The K^{*0} (m_0 = 896.1 MeV) and the $K^{*\pm}$ (m_0 = 891.6 MeV) are parametrized with the mass of the charged one and have an offset for the neutral $K^\star$. If fitted, the mass difference comes out to be 7 ± 2 MeV. The mass value of the $K^{\star\pm}$ is found in all fits with the stable position $m_0 = 891 \pm 3$ MeV. One also has to distinguish the different systematics of the decay kaons: the $K^{*\pm}$ is expected to have a larger width than the neutral one, since the K_L is reconstructed as missing. Parametrizing the resolution in terms of a Breit-Wigner width reveals a difference in the mass of 6 ± 3 MeV, too. The width of the neutral K^* is 61 ± 3 MeV, stable in all fits performed.

- $\bar{\mathrm{p}}\mathrm{p}\ (^3\mathrm{S}_1) \to K^*(892)K,\ K^*(892) \to K\pi$ (fig. 46 fig. 47)

  Due to the symmetry of the angular distribution and the isospin decomposition the interference between the two K^* bands is constructive for the annihilation from the $I = 0$ $\bar{\mathrm{p}}\mathrm{p}$ initial state and destructive from the $I = 1$ initial state. From a comparison of the four K^* amplitudes (fig. 44,45,46,47) for S-state annihilation with the appearance in the data plot one expects a dominant contribution for transitions from the $^3\mathrm{S}_1$ $I = 1$ initial state.

- $\bar{\mathrm{p}}\mathrm{p}\ (^1\mathrm{S}_0) \to (K\pi)_S K,\ (K\pi)_S \to K\pi$ (fig. 48 fig. 49)

  The $(K\pi)_S$ wave is described by a K-matrix consisting of a sum of a resonance pole term plus a non-resonant background in terms of a polynomial:

$$\widehat{K} = \frac{g^2}{m_0^2 - m^2} + c_1 + c_2 \cdot m \tag{47}$$

  with the constants $c_1 = 1.45$ and $c_2 = -0.55$ from an adjustment of the corresponding T-matrix to the data from LASS [27]. The resonance mass extracted from the T-matrix is $m = (1428 \pm 10)$ MeV and the width $\Gamma = 380$ MeV compatible with LASS' own determination [27].

- $\bar{\mathrm{p}}\mathrm{p}\ (^1\mathrm{S}_0) \to \mathrm{a}_0(980)\ \pi,\ \mathrm{a}_0(980) \to K\mathrm{K}_L$ (fig. 50)

  The $a_0(980)$ lies close to threshold, which means at the border of the Dalitz plot. It is described with a Flatte formula. The parametrization is copied from the coupled channel analysis [26], where it was observed in its $\pi^0\eta$ decay.

$$\widehat{F} = \beta\, \frac{m_0\Gamma_1/\rho_1}{m_0^2 - m^2 - im_0\rho_1(\Gamma_1/\rho_1 + \Gamma_2/\rho_2)}\ . \tag{48}$$

  Here ρ_1 and ρ_2 are the two body phasespaces ($\rho_i = 2q_i/m$) for $\bar{\mathrm{K}}\mathrm{K}$ and $\pi\eta$. Fig. 51 shows the projection of the partial wave into the $\bar{\mathrm{K}}\mathrm{K}$ subsystem.

- $\bar{\mathrm{p}}\mathrm{p}\ (^1\mathrm{S}_0) \to a_0(1450)\ \pi,\ a_0(1450) \to K\mathrm{K}_L$ (fig. 52)

  In the analysis of the final state $\pi^0\pi^0\eta$ of $\bar{\mathrm{p}}\mathrm{p}$ annihilation at rest the resonance $a_0(1450)$ was needed for a satisfactory description of the Dalitz plot. It showed up at the high mass end of the $\mathrm{a}_0(980)$-band [1, 26]. In principle it belongs into the same K-matrix as the $\mathrm{a}_0(980)$, but the overlapp is not important between the two objects, so that we can discuss it here in terms of a Breit-Wigner amplitude. The mass and width are $m = 1480$ MeV and $\Gamma = 265$ MeV. If one releases the parameters in the fit to $\mathrm{K}^{\pm}\pi^{\mp}\mathrm{K}_L$, the values are found to be $m = 1489 \pm 10$ MeV and $\Gamma = 265 \pm 11$ MeV.

- $\underline{\bar{\mathrm{p}}\mathrm{p}\ (^1\mathrm{S}_0) \to \mathrm{a}_2(1320)\ \pi,\ \mathrm{a}_2(1320) \to K\mathrm{K}_L}$ (fig. 53)

  The $\mathrm{a}_2(1320)$ lies far away from the $\bar{\mathrm{K}}\mathrm{K}$ threshold. It is described by a relativistic Breit-Wigner formula. Its mass fitted freely comes out at $m = 1312 \pm 5$ MeV and width $\Gamma = 117 \pm 5$ MeV, compatible with PDG [24].

- $\underline{\bar{\mathrm{p}}\mathrm{p}\ (^3\mathrm{S}_1) \to \mathrm{a}_2(1320)\ \pi,\ \mathrm{a}_2(1320) \to K\mathrm{K}_L}$ (fig. 54)

  Since the angular distributions of the $\mathrm{a}_2(1320)$ from $^3\mathrm{S}_1$ and $^1\mathrm{S}_0$ are quite different (see table 8) one is sensitive to the different contributions. From measurements of $\mathrm{a}_2(1320)$ in $\pi\pi\eta$ [30] one expects a factor of 3 increased $\mathrm{a}_2(1320)$ production from the $^1\mathrm{S}_0$ initial state.

- $\underline{\bar{\mathrm{p}}\mathrm{p}\ (^1\mathrm{S}_0) \to \rho\ \pi,\ \rho \to K\mathrm{K}_L}$ (fig. 55)

  We use a K-matrix with two poles according to the expectation, that there are two radial excitations of the $\rho(770)$. The $\bar{\mathrm{K}}\mathrm{K}$ coupling should be small.

- $\underline{\bar{\mathrm{p}}\mathrm{p}\ (^3\mathrm{S}_1) \to \rho\ \pi,\ \rho \to K\mathrm{K}_L}$ (fig. 56)

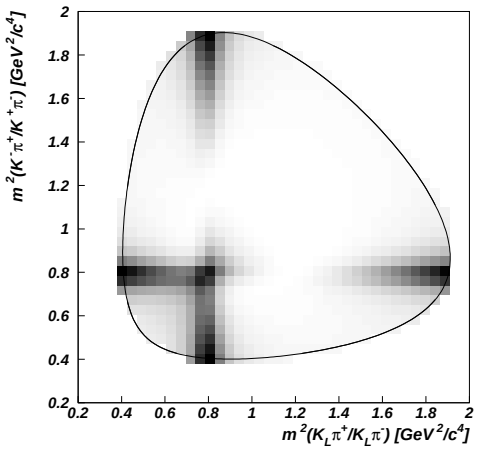

Figure 44: Simulation of the density distribution for $\bar{\mathrm{p}}\mathrm{p}$ $(^1\mathrm{S}_0) \to K^*(892)\,K$, $K^*(892) \to K\pi$ with isospin $I_{\overline{p}p} = 0$.

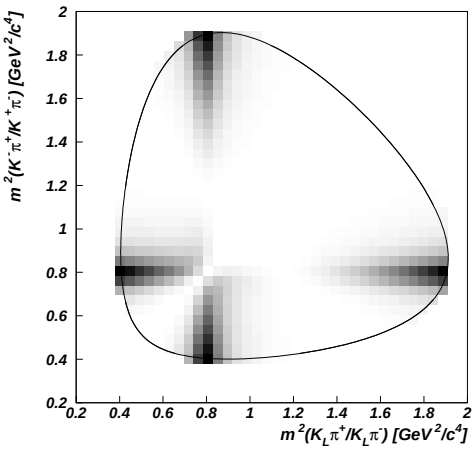

Figure 45: Simulation of $\bar{\mathrm{p}}\mathrm{p}$ $(^1\mathrm{S}_0) \to K^*(892)\;\;K,\;\; K^*(892) \to K\pi$ with isospin $I_{\overline{p}p} = 1$.

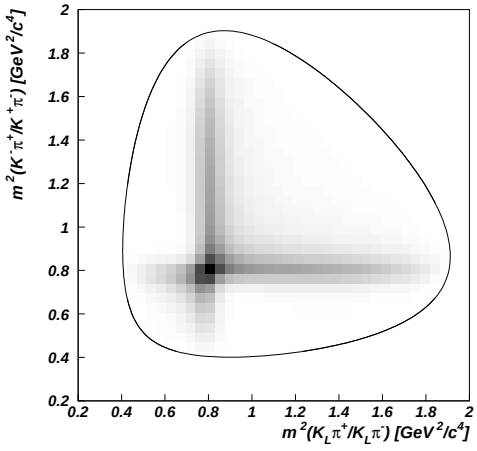

Figure 46: Simulation of $\bar{\mathrm{p}}\mathrm{p}$ $(^3\mathrm{S}_1) \to K^*(892)\;\;K,\;\; K^*(892) \to K\pi$ with isospin $I_{\overline{p}p} = 0$.

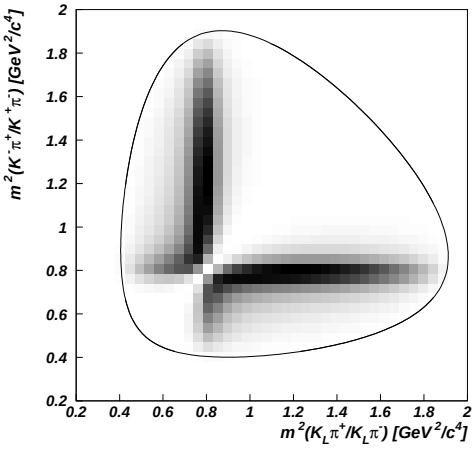

Figure 47: Simulation of $\bar{\mathrm{p}}\mathrm{p}$ $(^3\mathrm{S}_1) \to K^*(892)\;\;K,\;\; K^*(892) \to K\pi$ with isospin $I_{\overline{p}p} = 1$.

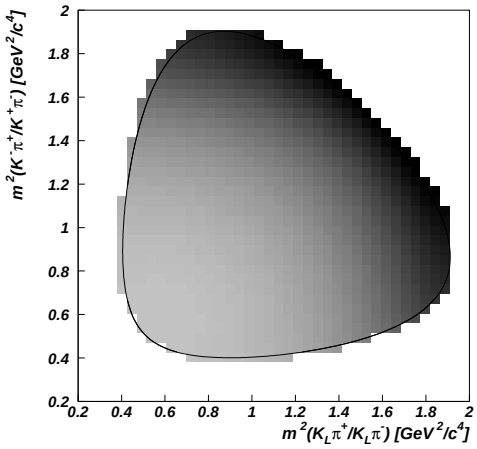

Figure 48: Simulation of $\bar{\mathrm{p}}\mathrm{p}$ $(^1\mathrm{S}_0) \rightarrow K_0^*$ (1430) K, K_0^* (1430) $\rightarrow K\pi$ mit $I_{\overline{p}p} = 0$.

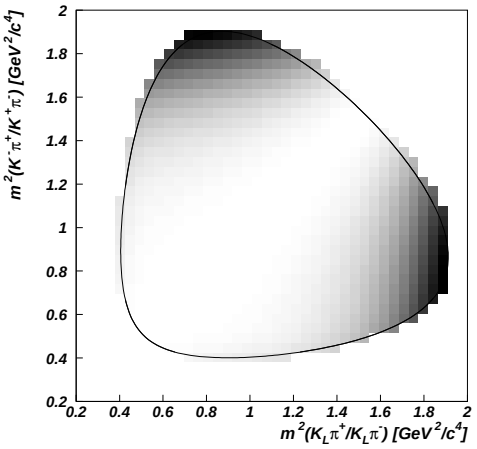

Figure 49: Simulation of $\bar{\mathrm{p}}\mathrm{p}$ $(^1\mathrm{S}_0) \rightarrow K_0^*$ (1430) K, K_0^* (1430) $\rightarrow K\pi$ mit $I_{\overline{p}p} = 1$.

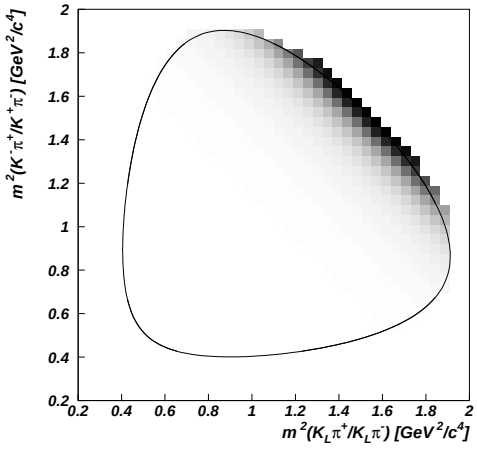

Figure 50: Simulation of $\bar{\mathrm{p}}\mathrm{p}$ $(^1\mathrm{S}_0) \rightarrow$ $\mathrm{a}_0(980)$ π, $\mathrm{a}_0(980) \rightarrow K\mathrm{K}_L$.

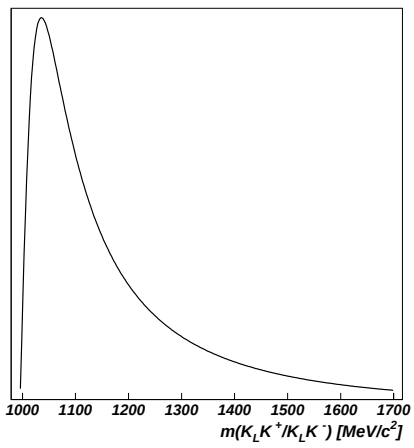

Figure 51: Projektion of the simulated density distribution for $\mathrm{a}_0(980)$ into the $\mathrm{K}_L\mathrm{K}^{\pm}$ subsystem.

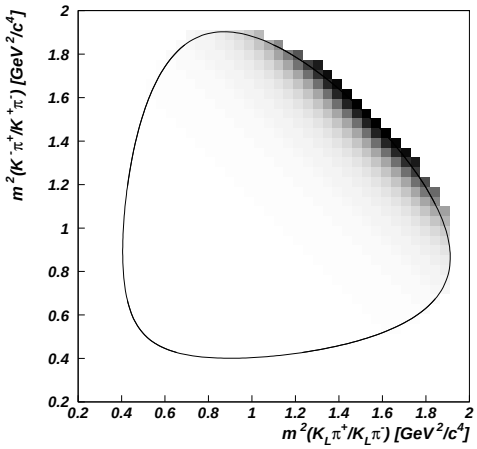

Figure 52: Simulation of $\bar{\mathrm{p}}\mathrm{p}$ $(^1\mathrm{S}_0) \rightarrow$ $a_0(1450)$ π, $a_0(1450) \rightarrow K\mathrm{K}_L$.

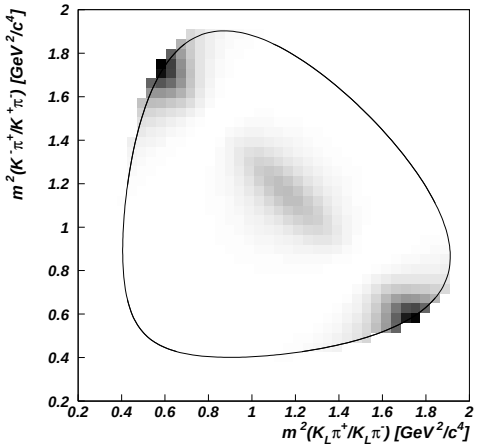

Figure 53: Simulation of $\bar{\mathrm{p}}\mathrm{p}$ $(^1\mathrm{S}_0) \rightarrow$ $\mathrm{a}_2(1320)$ π, $\mathrm{a}_2(1320) \rightarrow K\mathrm{K}_L$.

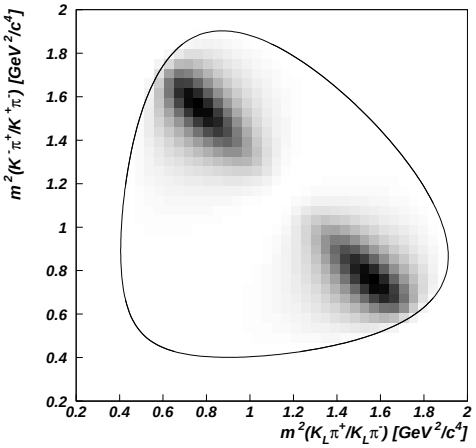

Figure 54: Simulation of $\bar{\mathrm{p}}\mathrm{p}$ $(^3\mathrm{S}_1) \rightarrow$ $\mathrm{a}_2(1320)$ π, $\mathrm{a}_2(1320) \rightarrow K\mathrm{K}_L$.

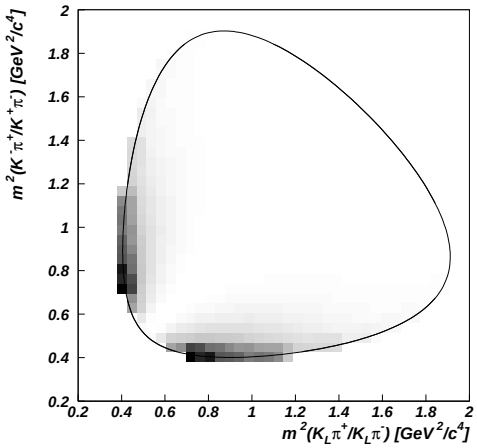

Figure 55: Simulation of $\bar{\mathrm{p}}\mathrm{p}$ ($^1\mathrm{S}_0$) $\rightarrow$ $\rho(1450)$ π, $\rho \rightarrow \bar{\mathrm{K}}\mathrm{K}$.

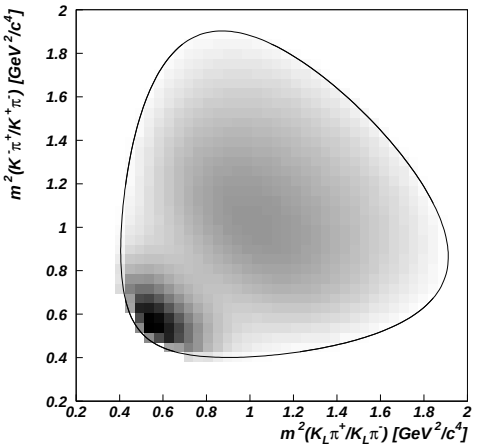

Figure 56: Simulation of $\bar{\mathrm{p}}\mathrm{p}$ ($^3\mathrm{S}_1$) $\rightarrow$ $\rho(1450)$ π, $\rho \rightarrow \bar{\mathrm{K}}\mathrm{K}$.

8 PWA fits

We now present the first fit based on well established resonances only. The $K^\star(892)$ resonance is parametrized as a relativistic Breit-Wigner amplitude since only the $K\pi$ channel is open. The charged $K^{\star\pm}$ mass is found in all fits with the stable position $m_0 = (891 \pm 3)$ MeV/c^2 and $\Gamma_0 = (61 \pm 3)$ MeV/c^2. The freely fitted mass difference between $K^{\star 0}$ and $K^{\star\pm}$ is $\Delta m = (7 \pm 2)$ MeV/c^2. The width is affected by the mass resolution $\sigma_m = 12$ MeV/c^2 at the $K^\star$ mass, according to simulation. Unfolding the Breit-Wigner into a Breit-Wigner and a Gaussian (Voigtian function) gives a resonance width of $m = (52 \pm 3)$MeV/c^2. The parameters agree well with measurements of other experiments [32].

The enhancement at the $\bar{\mathrm{K}}\mathrm{K}$ threshold is generated by the $a_0(980)$ resonance which couples to $\pi\eta$ and $\bar{\mathrm{K}}\mathrm{K}$. Therefore, it is parametrized by a 2×2 K-matrix reducing to the well known Flatté formula [33]:

$$F_0 = \beta_0' \frac{\begin{pmatrix} g_1 \\ g_2 \end{pmatrix}}{m_0^2 - m^2 - i(\rho_1 g_1^2 + \rho_2 g_2^2)} \; . \tag{49}$$

It was already applied to the $\pi^0\pi^0\eta$ Dalitz plot [1, 30] for which $g_1 = g_{\pi\eta}$ was determined to be $g_1 = 353$ MeV. The information about the two couplings in the $\pi\eta$ channel was extracted from the cusp-like shape of the $\pi\eta$ intensity which is caused by the opening of the $\bar{\mathrm{K}}\mathrm{K}$ threshold and introduces a correlation between the couplings.

For the $a_2(1320)$ we used a relativistic Breit-Wigner amplitude. It can be produced from the $(I = 0)$ $^1\mathrm{S}_0$ $\bar{\mathrm{p}}\mathrm{p}$ initial state - the angular distributions has a W shape - and the $(I = 1)$ $^3\mathrm{S}_1$ initial state - a U-shaped angular distribution peaking at the Dalitz plot boundary (see generics).

In addition to the vector $(K^\star)$ wave we expect a scalar $I = \frac{1}{2}$ S-wave which contains the $K^\star(1430)$. The parameters of the $(K\pi)$ S-wave were determined by fitting a scattering amplitude $T = \frac{1}{\rho} sin\delta \cdot e^{i\delta}$, based on the K-matrix to the phase shift of the LASS experiment [27]. It is purely elastic in the region of interest. We used the following ansatz:

$$K = \frac{g^2}{m_0^2 - m^2} + c_1 + c_2 m \tag{50}$$

This form also includes the low-energy $(K\pi)$ scattering. The fit yielded the constants $c_1 = 1.45$ and $c_2 = -0.55$/GeV and $m_0 = (1342 \pm 10)$ MeV/c^2, $\Gamma_0 = (400 \pm 20)$ MeV/c^2. The resonance mass and width extracted from the T-matrix in the complex energy plane are $m = (1428 \pm 10)$ MeV/c^2 and $\Gamma = (180 \pm 15)$ MeV/c^2, in close agreement with LASS [27]. In the Dalitz plot analysis

these values were then fixed. Alternatively, the K-matrix was formulated in terms of a scattering length including one resonance pole:

$$K = \frac{am}{2 + abq^2} + \frac{g_0^2}{m_0^2 - m^2} \tag{51}$$

with a the scattering length and b the effective range. A fit of this form gives $a = (2.58 \pm 0.21)$ GeV^{-1} and $b = (1.81 \pm 0.25)$ GeV^{-1}. The K-matrix values (m_0, Γ_0) and the T-matrix pole are, within errors, the same as before. For the transition from the $I = 1$ ^{1}S$_0$ state one obtains destructive interference between the two charges, from ^{1}S$_0$ $I = 0$ the interference is constructive. The fit to the data shows that the pole-term in the K-matrix is the dominant part. The $I = 1$ ^{1}S$_0$ initial state can also decay via the $I = \frac{3}{2}$ $K\pi$ S-wave. So far no resonance has been observed in this system [32]. If the $I = \frac{3}{2}$ wave has a similar energy dependence as the $I = \frac{1}{2}$ wave, they cannot be distinguished in the $K^0 K^{\pm}\pi^{\mp}$ final state. Hence we refrain from including it.

With this minimal hypothesis requiring 29 free parameters the fit led to a $\chi^2/N_{dof} = 1380/(730 - 29)$. It is not a satisfactory description since systematic deviations between theory and data are observed in the Dalitz plot. In particular, the region for $\bar{\text{K}}$K masses above the $a_2(1320)$ band is not described properly, as can be seen by the excess of predicted events in fig. 57. The $a_2(1320)$ mass position tends to a value below 1300 MeV/c^2. This phenomenon was already observed in the bubble chamber analyses [29, 34].

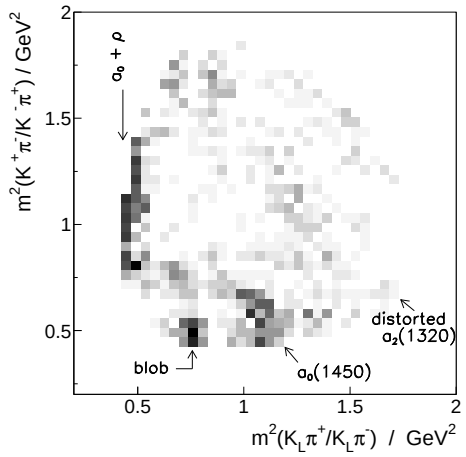

Figure 57:
Discrepancy over the Dalitz plot for the minimum hypothesis. The marked features are the lack of intensity at low $K\pi$ masses and at the $a_0(1450)$ position, the distorted $a_2(1320)$ band and the blob in the $K^{\star\pm}(892)$ band.

In the next step we introduced a pole for the $a_0(1450)$ in the K-matrix in addition to $a_0(980)$. Since the $\pi\eta$ and $\bar{\text{K}}$K thresholds are far away we see no significant influence on the line shape of the $a_0(1450)$ and therefore need coupling to $\bar{\text{K}}$K only. The quality of the description improves significantly to $\chi^2/N_{dof} =$

$969/(730-33)$. Two aspects give further confidence in the introduction of this resonance: First, the $a_2(1320)$ is now found at a mass of $m = 1312 \pm 5$ MeV/c^2 and with a width of $\Gamma = 117 \pm 5$ MeV/c^2, in good agreement with our analysis of the $\pi^0\pi^0\eta$ final state. Secondly, the mass and width of the $a_0(1450)$ are fitted to $m = 1489 \pm 10$ MeV/c^2 and $\Gamma = 265 \pm 11$ MeV/c^2, respectively. This agrees with the analysis of $\pi^0\pi^0\eta$ [1, 30]. For the $^1S_0$ initial state, the strength of $a_2(1320)$ is correlated with the strength of $a_0(1450)$: for an $a_2(1320)$ contribution increasing from 11% to 15% the $a_0(1450)$ increases from 8% to 13% while χ^2 changes by about $\Delta\chi^2 = 10$.

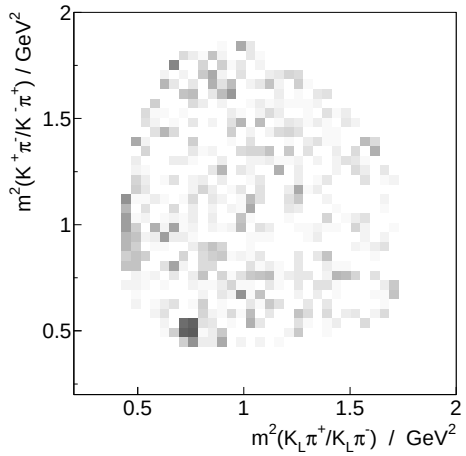

Figure 58:
χ^2 distribution over the Dalitz plot after inclusion of $a_0(1450)$.

Still, we are left with a discrepancy in fig. 57 evidenced by the blob in the $K^{\star\pm}$ band at low $K^\pm\pi^\mp$ masses (see χ^2 distribution fig. 58). The interference between the $K^\star$ bands does not explain all of the observed intensity. The difference could be due to a resonance in the $\bar{K}K$ system at high mass which runs through the $K^\star$ band. The maximum intensity close to the Dalitz plot edge is due to a higher spin. A candidate is the radial excitation of the $a_2(1320)$, the $a_2(1680)$, which was already introduced in $\pi^0\pi^0\eta$ [1]. The fit to $K^\pm\pi^\mp K_L$ accepts the additional pole to the $a_2(1320)$ in the $\bar{K}K$ D-wave with an improvement in the χ^2 of 50, although the width takes unreasonable values below 50 MeV/c^2. Also, one expects suppression of a spin-2 resonance close to the end of phase space ($m = 1740$ MeV/c^2) due to the centrifugal barrier in the production. With spin 1 instead, the mass position decreases to about 1600 MeV/c^2 and the width becomes $\Gamma \approx 200$ MeV/c^2. The χ^2 decreases significantly by $\Delta\chi^2 = 160$ and the blob is now described satisfactorily. The χ^2 distribution is shown in fig. 59

The observation of a vector meson with a mass above 1400 MeV/c^2 decaying into $\bar{K}K$ was reported in the reaction $\pi^\pm p \to K_S K^\pm p$ at 30 GeV/c and 50 GeV/c [35]. Two radial excitations of the $\rho(770)$ are known [32], the $\rho(1450)$

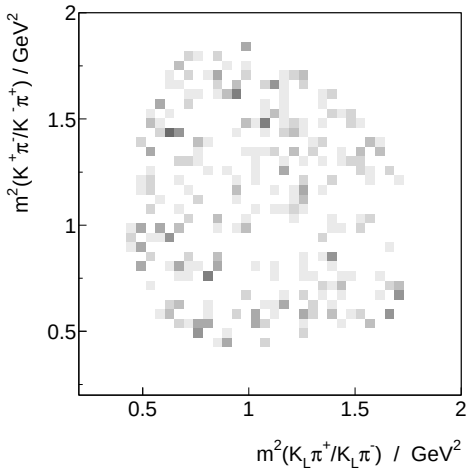

Figure 59:
The χ^2 distribution over the Dalitz plot for the best hypothesis is flat. The scaling of colours is the same as in fig. 6.

and the $\rho(1700)$. These resonances were also reported by our collaboration, decaying to $\pi^-\pi^0$ in $\bar{p}n \to \pi^-\pi^0\pi^0$ in liquid deuterium [36]. We therefore try a two-pole K-matrix for the $\bar{\mathrm{K}}\mathrm{K}$ P-wave, $(m_\alpha, \Gamma_\alpha) = (1430\ \mathrm{MeV/c^2}\ ,\ 170\ \mathrm{MeV/c^2})$ and $(1740\ \mathrm{MeV/c^2}\ ,\ 190\ \mathrm{MeV/c^2})$), which reproduces the T-matrix poles in [36]. The data demand a single structure around 1600 MeV/c^2 in the Dalitz plot which the fit achieves by appropriate choice of the production strengths and phases. Hence, we name it $\rho(1600)$. The χ^2 remains at $\chi^2/N_{dof} = 810/(730-45)$. In this fit the mass of the $a_0(1450)$ can be moved between 1450 MeV/c^2 and 1510 MeV/c^2 changing χ^2 by only 20. The width of the $a_0(1450)$ is relatively stable, and hence we quote $m = (1480 \pm 30)$ MeV/c^2 and $\Gamma = (265 \pm 15)$ MeV/c^2. This is the best fit that can be achieved with the channel $\mathrm{K}^\pm\pi^\mp\mathrm{K}_L$ only.

The intensity distribution of $\rho(1600)$ ($\rho(1450)+\rho(1700)$) produced from $^1\mathrm{S}_0$ $\bar{\mathrm{p}}\mathrm{p}$ initial state. shows maxima at positions where the discrepancies in the Dalitz plot are obsereved. The form of the deviations is created by the interference with the $K^\star(892)$ amplitudes and the $a_0(1450)$ amplitude. The data are rather insensitive to the intensity enhancement of the transition $A(\bar{\mathrm{p}}\mathrm{p}(^3\mathrm{S}_1) \to\ \rho^\pm\pi^\mp; \rho \to \mathrm{K}_L K^\pm)$ at high $\mathrm{K}_L K^\pm$ masses. Information about the production of $\rho(1600)$ from $^3\mathrm{S}_1$ originates from all over the Dalitz plot area where it easily pickes up some intensity from the likewise extended $K\pi$ S-wave produced from $^1\mathrm{S}_0$.

9 Discussion

The production parameters for the best fit are compiled in table 1 and the theoretical Dalitz plot is displayed in fig. 60. The fit quality can be seen from the mass projections (fig. 60) with the fitted intensity distribution superimposed.

The fit requires about 60% from $^1\mathrm{S}_0$ and about 40% from $^3\mathrm{S}_1$. It is instructive

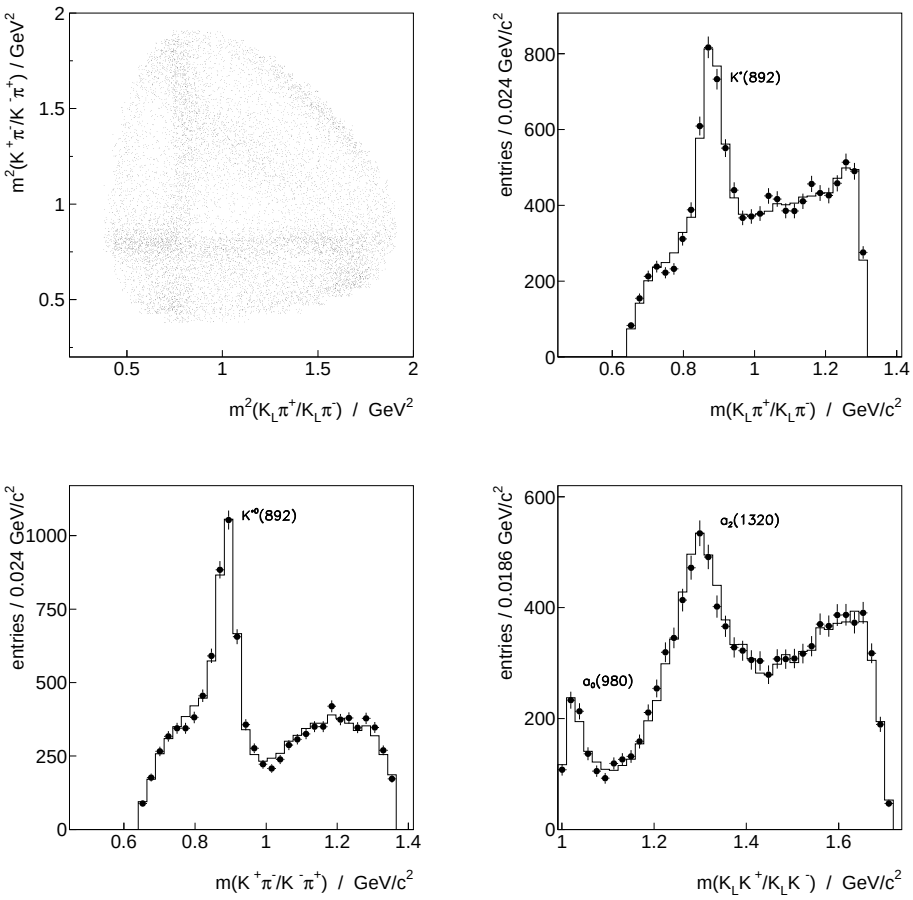

Figure 60: *Theoretical Dalitz plot corresponding to the best fit, and the mass projections with the fit (line) superimposed to the data (dots).*

to compare the production of the meson resonances with previous measurements. For the normalization of the partial branching ratios compiled in table 2 we take the average of total branching ratios from the bubble chambers [9, 34] and this analysis:

$$B(\bar{\mathrm{p}}\mathrm{p} \to \mathrm{K}^{\pm}\pi^{\mp}\mathrm{K}_L) = (2.74 \pm 0.10) \cdot 10^{-3}\,. \tag{52}$$

Our absolute branching ratios for decays into $\bar{K}K\pi$ are given in table 2.

The relative production of $K^{\star}(892)\bar{K} \pm \bar{K}^{\star}(892)K$ from $^3\mathrm{S}_1$ to $^1\mathrm{S}_0$ is $r = 3.0 \pm 0.6$ in agreement with the previous determination from Bettini et al. [29] $r = 2.4 \pm 0.5$. As in the bubble chamber experiment we have integrated the coherent

resonance	$I(\bar{\mathrm{p}}\mathrm{p})$	relative intensity [%]	a	$\phi\ [rad]$
$\boldsymbol{^1S_0}$		62 ± 5		
$K^*(892)$	0	7.5 ± 1.0	-1.45	0.0
	1	1.1 ± 0.4	0.64	3.9
$(K\pi)_S$-Welle	0	30.3 ± 7.0	-2.49	6.0
	1	4.7 ± 2.0	3.45	5.5
$\mathrm{a}_0(980)$	0	$7.2^{+0.5}_{-1.2}$	12.53	0.4
$a_0(1450)$	0	10.8 ± 2.0	1.27	4.6
$\rho(1600)$	1	$3.2^{+0.5}_{-1.0}$	0.60/1.72	3.8/5.9
$\mathrm{a}_2(1320)$	0	$14.6^{+1.0}_{-3.0}$	2.30	4.3
sum		79.4 ± 8.0		
$\boldsymbol{^3S_1}$		38 ± 4		
$K^*(892)$	0	5.5 ± 1.5	0.87	0.0
	1	20.2 ± 3.0	1.97	5.3
$\rho(1600)$	0	3.2 ± 1.0	-0.4/1.3	0.1/2.2
$\mathrm{a}_2(1320)$	1	5.2 ± 1.6	1.10	5.4
sum		34.1 ± 3.8		
total sum		113.5 ± 8.9		

Table 9: The resonance contributions and the relative production phases. Negative a means a phase offset of π.

sum of the $K^\star$ amplitude and its charge conjugate [29, 34]. If the interference between the two $K^\star$ bands is neglected slightly modified intensities are obtained. This causes, however, a drastic change for the contribution of the $K^\star(1430)$ which extends over the whole Dalitz plot. Since destructive interference removes most of the wave produced from the $I = 1$ initial state, one obtains a much higher intensity by integrating the two $K^\star(1430)$ branches independently: instead of $(4.7 \pm 2.0)\%$ we get $2 \times (20.0 \pm 8.5)\%$. For the transition from the $I = 0$ initial state we have individual contributions of $2 \times (7.8 \pm 1.8)\%$ instead of $(30.3 \pm 7.0)\%$. For broad objects the branching ratios are a matter of definition and should not, therefore, be taken at face value. The strong $K\pi$ S-wave has already been noticed in ref. [28]. In fact, from our observations [26] we expect annihilation from S-states into any three pseudoscalars to proceed dominantly through two-body 0^{++}

$^1S_0$	$B(\bar{p}p \to R\pi \to \bar{K}K\pi) \cdot 10^4$	
$a_0(980)$		$5.92\ ^{+0.46}_{-1.01}$
$a_0(1450)$		8.88 ± 1.68
$\rho(1600)$		$1.75\ ^{+0.28}_{-0.55}$
$a_2(1320)$		$12.00\ ^{+0.93}_{-2.53}$
$^1S_0$	$B(\bar{p}p \to RK \to \bar{K}K\pi) \cdot 10^4$	
$K^\star(1430)$	$I_{\bar{p}p} = 0$	24.91 ± 5.83
	$I_{\bar{p}p} = 1$	3.86 ± 1.65
$K^\star(892)$	$I_{\bar{p}p} = 0$	6.17 ± 0.85
	$I_{\bar{p}p} = 1$	0.90 ± 0.33
$^3S_1$	$B(\bar{p}p \to R\pi \to \bar{K}K\pi) \cdot 10^4$	
$\rho(1600)$		2.63 ± 0.83
$a_2(1320)$		2.85 ± 0.88
$^3S_1$	$B(\bar{p}p \to RK \to \bar{K}K\pi) \cdot 10^4$	
$K^\star(892)$	$I_{\bar{p}p} = 0$	4.52 ± 1.24
	$I_{\bar{p}p} = 1$	16.60 ± 2.54

Table 10: Branching ratios of the meson resonances R contributing to $K_L K^\pm \pi^\mp$.

waves.

The intensity at the $\bar{\mathrm{K}}\mathrm{K}$ threshold is attributed to the $a_0(980)$, which we also observed in the annihilation channel $\pi^0\pi^0\eta$ with a branching ratio of $B(\bar{\mathrm{p}}\mathrm{p}(^1\mathrm{S}_0) \to a_0(980)\pi; a_0 \to \pi\eta) = (2.61 \pm 0.48) \cdot 10^{-3}$ [1]. Since the resonance lies extremely close to the threshold of the $\bar{\mathrm{K}}\mathrm{K}$ channel, its apparent intensity distribution in $\bar{\mathrm{K}}\mathrm{K}$ and $\pi\eta$ is very much different from that of a Breit-Wigner. Fig. 61 shows its cusp-like shape for the $\pi\eta$ channel and in hatched style the intensity distribution in $\bar{\mathrm{K}}\mathrm{K}$, where $a_0(1450)$ is neglected. For this plot we have recalculated the Flatté amplitude F, eq. (49) and corrected for two-body phase space. From table 2 and ref. [1] we calculate the ratio of branching ratios:

$$r(a_0(980)) = \frac{B(\bar{\mathrm{p}}\mathrm{p} \to a_0\pi; a_0 \to \bar{\mathrm{K}}\mathrm{K})}{B(\bar{\mathrm{p}}\mathrm{p} \to a_0\pi; a_0 \to \pi\eta)} = 0.23 \pm 0.05\ . \tag{53}$$

Realize, that a factor 3 for all $\pi\eta$ modes is included. The ratio of couplings to $\pi\eta$ and $\bar{\mathrm{K}}\mathrm{K}$ is extracted by fitting eq. (49) with the constraint that the ratio of the integrated intensities is equal to our fit result eq. (53). The K-matrix pole was determined in the Dalitz plot analysis to be $m_0 = (999 \pm 2)$ MeV/c^2 and was fixed for this procedure. We obtain the coupling $g_{\pi\eta} = g_1 = 324 \pm 5$ MeV and a ratio

of couplings $r = g_2/g_1 = 1.03 \pm 0.14$. This compares well with our estimate in [1] even though there we had to rely on the line shape to extract information about the $\bar{\mathrm{K}}\mathrm{K}$ partial width. In the present procedure the constraining information on the couplings is the number of events attributed to the $a_0(980)$ which is rather insensitive to the mass resolution. The pole positions in the complex energy plane corresponding to the parameters above are: in Riemann sheet II $(m - i\Gamma/2) = (982 - i46)$ MeV/c^2 and in sheet III $(1006 - i49)$ MeV/c^2. The relevant value closest to the physical sheet for an object appearing as a resonance below the second threshold is sheet II, and hence we obtain a mass and a width for the $a_0(980)$, including the uncertainties from the underlying parameters: $m = 982 \pm 3$ MeV/c^2 and $\Gamma = 92 \pm 8$ MeV/c^2.

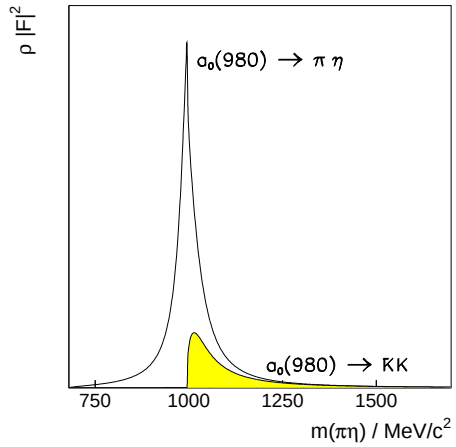

Figure 61:
The amplitudes $\rho_{\pi\eta}|F_{\pi\eta}|^2$ *and* $\rho_{\bar{K}K}|F_{\bar{K}K}|^2$ *(shaded area).*

We have introduced the $a_0(1450)$ into the same K-matrix, but have not considered its coupling to the $\pi\eta$ channel, since it is far away from both thresholds. We have probed the significance of this resonance by fitting the Dalitz plot for fixed values of the $a_0(1450)$ contribution, leaving its mass and width at the values found for the best fit. The χ^2 dependence of the $a_0(1450)$ contribution is displayed in fig. 62. For a contribution of 0.5% the $\Delta\chi^2$ reaches 100; if $a_0(1450)$ is omitted $\Delta\chi^2 = 150$.

From SU(3)-flavour assuming that $a_0(1450)$ is the pure $\bar{q}q$ octett state and the relative creation of $\bar{u}u$ or $\bar{d}d$ versus $\bar{s}s$ is equal probable we predict the relative coupling of the $a_0(1450)$ to $\bar{\mathrm{K}}\mathrm{K}$ and $\pi\eta$:

$$r_1(a_0(1450)) = \frac{B(a_0 \to \bar{\mathrm{K}}\mathrm{K})}{B(a_0 \to \pi\eta)} = \frac{1}{2\,\cos^2\phi}\,\frac{q_{\bar{K}K}}{q_{\pi\eta}}\,, \tag{54}$$

where $\phi = 54.7^o + \theta_{PS}$. With a pseudoscalar mixing angle of $\theta_{PS} = -(17.3 \pm$

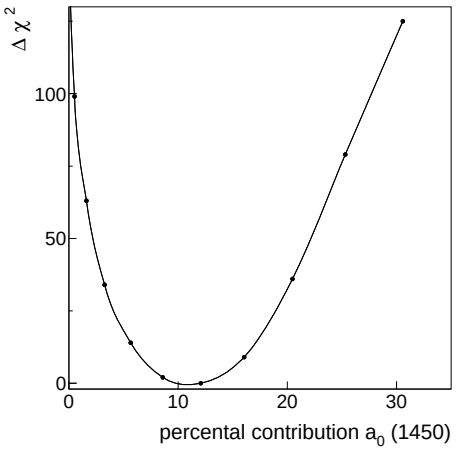

Figure 62:
χ^2-scan for different intensities of $a_0(1450)$.

$1.8)^o$ [37] and phase space evaluated at $m = 1480$ MeV/c^2 we obtain:

$$r_1(a_0(1450)) = 0.69 \pm 0.03\,. \tag{55}$$

The error is determined by the uncertainty in the pseudoscalar mixing angle. With the branching ratio $B(\bar{\mathrm{p}}\mathrm{p}(^1\mathrm{S}_0) \to a_0\pi; a_0 \to \pi\eta) = (10.05 \pm 1.80) \cdot 10^{-4}$ [1] we obtain:

$$r_1(a_0(1450)) = 0.88 \pm 0.23\,, \tag{56}$$

which agrees with eq. (55). Recently, we also published the branching ratio for the $\pi^0\eta'$ decay of this resonance extracted from the partial wave analysis of the final state $\pi^0\pi^0\eta'$ of $\bar{\mathrm{p}}\mathrm{p}$ annihilation at rest [31]. Summarizing, we find the following ratios of branching ratios compared to flavour SU(3):

	$\pi\eta$	$\bar{\mathrm{K}}\mathrm{K}$	$\pi\eta'$
SU(3)	1.	0.69±0.03	0.39±0.04
Crystal Barrel	1.	0.88±0.23	0.35±0.16

The isovector scalar resonance $a_0(1450)$ is well described by the decay pattern predicted by flavour SU(3). Hence, it naturally finds its place in the 0^{++} nonet.

We now compare the branching ratio of $a_2(1320)$ $B(\bar{\mathrm{p}}\mathrm{p}\ (^1\mathrm{S}_0\,, ^3\mathrm{S}_1) \to a_2\pi; a_2 \to \bar{\mathrm{K}}\mathrm{K}) = (14.85 \pm 1.94) \cdot 10^{-4}$ from this analysis with the values from bubble chambers $(8.7 \pm 2.0) \cdot 10^{-4}$[28] and $(12.4 \pm 1.9) \cdot 10^{-4}$[29]. Both found an $a_2(1320)$ mass below 1300 MeV. We explain this mass shift by the interference with $a_0(1450)$. For the ratio of $a_2(1320)$ production from the initial states $^1\mathrm{S}_0$ and $^3\mathrm{S}_1$ we get:

$$f = \frac{B(\bar{\mathrm{p}}\mathrm{p}(^1\mathrm{S}_0) \to a_2\pi)}{B(\bar{\mathrm{p}}\mathrm{p}(^3\mathrm{S}_1) \to a_2\pi)} = 4.2^{+1.3}_{-1.6}\,, \tag{57}$$

compared to $f = 3.0 \pm 1.5$ from ref. [28]. However, we do not attach much significance to this agreement because of the large errors. The relative decay ratio of $a_2(1320)$ from the present analysis and the $\pi^0\pi^0\eta$ result $B(\bar{\mathrm{p}}\mathrm{p}{\to}a_2(1320)\pi^0; a_2(1320){\to}\pi^0\eta) = (1.9 \pm 0.3) \cdot 10^{-3}$ [1] is:

$$r_1(a_2(1320)) = \frac{B(a_2{\to}\ \bar{\mathrm{K}}\mathrm{K})}{B(a_2{\to}\ \pi\eta)} = 0.21^{+0.04}_{-0.06}\,. \tag{58}$$

According to PDG [32] this quantity being $r_1(a_2(1320)) = 0.34 \pm 0.06$ is slightly higher. In the recent analysis of the reaction $\bar{\mathrm{p}}\mathrm{p} \to \pi^0\pi^0\eta'$ [31] we found $B(\bar{\mathrm{p}}\mathrm{p} \to a_2(1320)\pi^0; a_2{\to}\ \pi^0\eta') = (6.4 \pm 1.3) \cdot 10^{-5}$, which gives a relative decay ratio:

$$r_2(a_2(1320)) = \frac{B(a_2{\to}\ \pi\eta')}{B(a_2{\to}\ \pi\eta)} = 0.034 \pm 0.009\ , \tag{59}$$

while PDG gives $r_2(a_2(1320)) = 0.039 \pm 0.008$. Both agree.

Let us now discuss the impact of the present analysis on the interpretation of the $I = 0$ scalar resonance $f_0(1500)$, which we have observed earlier in different final states. The $f_0(1500)$ contribution to the final state $\mathrm{K}_L\mathrm{K}_L\pi^0$ of $\bar{\mathrm{p}}\mathrm{p}$ annihilation at rest depends on the contribution of $a_0(1450)$ [7] (see fig. 63). The branching ratio for $f_0(1500)$ is determined to be $B(\bar{\mathrm{p}}\mathrm{p} \to f_0(1500)\pi; f_0(1500){\to}\ \bar{\mathrm{K}}\mathrm{K}) = (4.52 \pm 0.36) \cdot 10^{-4}$. SU(3) flavour symmetry predicts for a pure $\bar{s}s$ meson a coupling of $\bar{\mathrm{K}}\mathrm{K}$ relative to $\pi\pi$ of $r = \infty$ and for a $(\bar{u}u + \bar{d}d)$ meson $r = \frac{1}{3}$. With the $B(\bar{\mathrm{p}}\mathrm{p} \to f_0(1500)\pi; f_0(1500){\to}\ \pi^0\pi^0) = (1.27 \pm 0.33) \cdot 10^{-4}$ [26] we calculate:

$$r = \frac{1}{3}\frac{B(f_0{\to}\ \bar{\mathrm{K}}\mathrm{K})}{B(f_0{\to}\ \pi^0\pi^0)} \cdot \frac{q_{\pi\pi}}{q_{\bar{K}K}} = 0.15 \pm 0.04 \tag{60}$$

Ratio (60) makes the interpretation of $f_0(1500)$ as $\bar{s}s$ meson rather unlikely. Its decay pattern is similar to that of a $(\bar{u}u + \bar{d}d)$ meson (the SU(3) limit is drawn in (fig. 63) for ideal mixing). The scalar nonet can be constructed from Crystal Barrel investigations with $f_0(1370)(I = 0)$, $a_0(1450)(I = 1)$ and $K^\star(1430)(I = \frac{1}{2})$ [41]. Therein, the position of the ω - like partner of a nonet is already occupied by $f_0(1370)$. The supernumerary status of $f_0(1500)$ is supported by its small width compared to the nonet members [39, 40]. The glueball interpretation of the $f_0(1500)$ based on its couplings is discussed in [42]. According to these calculations the ϕ - like scalar meson has to be found at masses above 1600 MeV/c^2. A possible candidate is the $f_J(1700)$ if its spin can be established to be $J = 0$ [32].

References

[1] C. Amsler et al, Phys. Lett. B333(1994) 277-282

[2] N. P. Hessey, Split-off Recognition with Dolby-C, CB-Note 182 (1992)

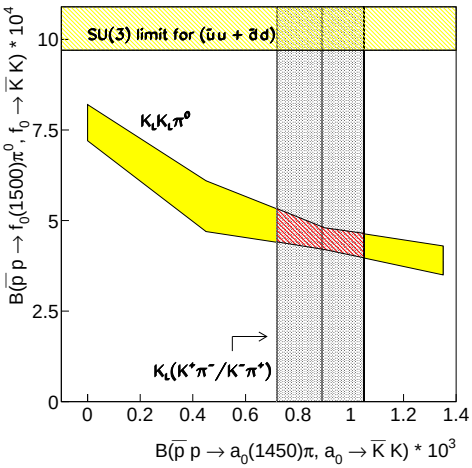

Figure 63:
Determination of the branching ratio of $f_0(1500)$ in the reaction $\bar{p}p \to K_L K_L \pi^0$ [7], where it is correlated with $a_0(1450)$ production. The $a_0(1450)$ contribution is fixed by the present measurement (dark hatched area). It cuts out a certain range of the $f_0(1500)$ ratio (light hatched area). The box at the top of the graph shows the lower SU(3) limit for a $(\bar{u}u + \bar{d}d)$ state in an ideally mixed 0^{++} nonet.

[3] M. Benayoun et al., Split-off Recognition in Data with charged Tracks. The TAXI Logics, CB-Note 280 (1995)

[4] W. R. Leo, Techniques for Nuclear und Particle Physics Experiments, Springer-Verlag (1994)
G. Grossmann, Computersimulation zur Trennung geladener Pionen und Kaonen mit dem Crystal Barrel Detektorsystem, Diplomarbeit Universität Karlsruhe (1989)

[5] P. Hidas and G. Pinter, Kinematic Fitting Software, CB-Note 138 (1995)

[6] R. Bossingham, Monte Carlo Software, CB-Note 169 (1992)

[7] S. v. Dombrowski, Proton-Antiproton Annihilation at Rest into $\pi^0 K_L K_L$, Dissertation Universität Zürich (1996)

[8] S. Ravndal and M. Goossens, GEANT, Detector Description and Simulation Tool, CERN Program Library Long Writeup W5013

[9] R. Armenteros et al., Phys. Lett. 17(1965) 170

[10] C. Amsler et al., Z. Phys. C58(1993) 175

[11] C. Strassburger, zur Verfügung gestellter Dalitzplot

[12] C. Amsler und F. Myhrer, Low Energy Antiproton Physics, CERN-PPE / 91 - 29 (1991)

[13] P. Weidenauer et al., Z. Phys. C47(1990) 353

[14] C. Voelcker, persönliche Mitteilung

[15] O. Kramer, Protonium-Vernichtung in $K_S K_L$, Diplomarbeit Universität München (1993)

[16] R. Bizzarri et al., Nucl. Phys. B14(1969) 169

[17] Kenneth M. Watson, Phys. Rev. **88**(1952) 1163

[18] S.U. Chung et al., Ann. Phys. **4** (1995) 404

[19] F. V. Hippel, C. Quigg, Phys. Rev. **5** (1972) 624

[20] J. D. Jackson, Nuovo Cimento 34(1964) 1644

[21] S. Spanier, COPWA: A Program for Coupled Channel Partial Wave Analysis, CB-Note 297 (1996)

[22] F.James and M. Roos, CERN Library long writeup D506, 1987

[23] S. Baker and D. Cousins, Nucl. Instr. Meth. **221**(1984) 437.

[24] Review of Particle Physics, Phys. Rev. **D54** (1996) 1

[25] G. Reifenröther and E. Klempt, Phys. Lett. B245(1990) 129

[26] C. Amsler et al., Phys. Lett. **B 355**(1995) 425

[27] D. Aston et al., Nucl. Phys. B296(1988) 493

[28] B. Conforto et al., Nucl. Phys. B3(1967) 469

[29] A. Bettini et al., Nuovo Cimento **78 A**(1969) 1199

[30] S. Spanier, Die Beobachtung einer isovektoriellen 0^{++} - Resonanz mit einer Masse von 1470 MeV/c^2 im $\pi^0\pi^0\eta$ - Endzustand der Proton - Antiproton - Vernichtung in Ruhe, Dissertation Universität Mainz (1994)

[31] A. Abele et al., Phys. Lett. **B 404** (1997) 179

[32] Review of Particle Physics, Phys. Rev. **D54** (1996) 1

[33] S.M. Flatté, Phys. Lett. **B 63**(1976) 224

[34] N. Barash et al., Phys. Rev. **6 B**(1965) 1659

[35] W.E. Cleland et al., Nucl. Phys. **B 208**(1982) 228

[36] A. Abele et al., Phys. Lett. **B 391**(1997) 191

[37] C. Amsler et al., Z. Phys. **C 42** (1993) 175

[38] P. Weidenauer et al., Z. Phys. **C 47**(1990) 353

[39] S. Godfrey and N. Isgur, Phys. Rev. **D 32**(1985) 189

[40] R. Kokoski and N. Isgur, Phys. Rev. **D 35**(1987) 907

[41] S. Spanier, Nucl. Phys. **B**(Proc. Suppl.)**54A**(1997) 362

[42] C. Amsler, F.E. Close, Phys. Rev. **D 53**(1996) 295